Geomorphology 434 (2023) 108732

Contents lists available at ScienceDirect

Geomorphology

journal homepage: www.journals.elsevier.com/geomorphology

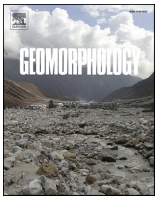

Morphometry and evolution of sinkholes on the western shore of the Dead Sea. Implications for susceptibility assessment

Jorge Sevil [*], Francisco Gutiérrez

Universidad de Zaragoza, Departamento de Ciencias de la Tierra, c. Pedro Cerbuna 12, 50009 Zaragoza, Spain

ARTICLE INFO

Keywords:
Salt karst
Subsidence
Hypogenic
Multi-temporal mapping
Coalescence
Susceptibility

ABSTRACT

Sinkhole development is a hazardous geomorphic process responsible for increasing economic losses worldwide. The highly dynamic eogenetic salt karst of the Dead Sea is one of the most striking examples of a human-enhanced sinkhole hazard. Since the 1980s, the shores of the Dead Sea have been affected by thousands of sinkholes while the lake level has been declining. Sinkholes pose a major threat, but their rapid development also offers an exceptional opportunity to study their evolution. Although the evolution of the morphometry and distribution of sinkholes provides essential data for hazard assessment, this kind of studies are almost lacking because of the typical slowness of the processes. Here we present multi-temporal cartographic sinkhole inventories of a sector in the western shore of the Dead Sea. The database was constructed using aerial and satellite imagery, high-resolution three-dimensional photogrammetric models, and fieldwork. Most of the depressions mapped were single, small, relatively shallow, subcircular, collapse sinkholes nested within large sagging basins. From 2005 to 2021, the 702 new sinkholes have been concentrated along a narrow N-S-oriented strip comprising tightly packed alignments and clusters. Sinkhole expansion by mass wasting and coalescence play an essential role in the evolution of the sinkhole landscape. An average subsidence rate of 45 cm/year has been calculated for the total area affected by sinkholes, providing an indirect estimate for the rate of subsurface salt dissolution. This research illustrates how multi-temporal geomorphic mapping and morphometric analyses provide an objective basis for the development of reliable spatial predictions for sinkhole evolution.

1. Introduction

Many karst regions throughout the world suffer significant economic losses related to sinkhole development. Very often the damaging sinkholes are induced or accelerated by human activities that alter the surface and/or underground hydrological systems (Gutiérrez, 2016; Parise, 2019; De Waele and Gutiérrez, 2022). The eogenetic salt karst of the Dead Sea is one of the most striking examples worldwide, with the development of thousands of human-induced sinkholes since 1980s in the expanding lake shores (Abelson et al., 2017). The extremely high activity of the subsidence phenomena poses a major threat, but also an exceptional opportunity to study the morphometric and spatio-temporal evolution of sinkholes using high-resolution data covering a limited time span.

The Dead Sea endorheic lake, the lowest continental area on Earth, has been affected by a water-level decline since 1950s. It used to be a single water body occupying the whole Dead Sea basin, but nowadays it is restricted to a northern sub-basin, and the southern one is occupied by evaporation ponds for potash extraction (Fig. 1a and b; Ben-Avraham et al., 2008). The Dead Sea water has a salinity of approximately 340 g/L (Al-Halbouni et al., 2021), around 9 times the salinity of the ocean water, and it is mostly saturated with respect to halite. In addition to the Jordan River, its main water input, the lake also receives water from three main aquifers (Kurnub sandstone aquifer, Judean carbonate aquifer, Quaternary alluvium) that discharge into the lake basin via springs located in the lake bottom or in the vicinity of the coastline (Yechieli et al., 1995, 2006; Abelson et al., 2006; Charrach, 2019). The lake level decline is mainly caused by water diversion from the Jordan River for irrigation, and pumping of Dead Sea water to feed the southern evaporation ponds (Closson et al., 2013; Abou Karaki et al., 2016). In the 1970s the lake level fell at a rate of 0.5 m/year, and in the last decade the decline rate has reached 1.1 m/year (Vey et al., 2021).

The contraction of the lake and the accompanying base-level drop have induced a number of hazardous geomorphic processes, such as landsliding, fluvial downcutting, and subsidence. The latter is related to three main types of processes: (1) widespread subsidence associated

---

* Corresponding author.
E-mail address: jorgesevil@unizar.es (J. Sevil).

https://doi.org/10.1016/j.geomorph.2023.108732
Received 9 March 2023; Received in revised form 9 May 2023; Accepted 9 May 2023

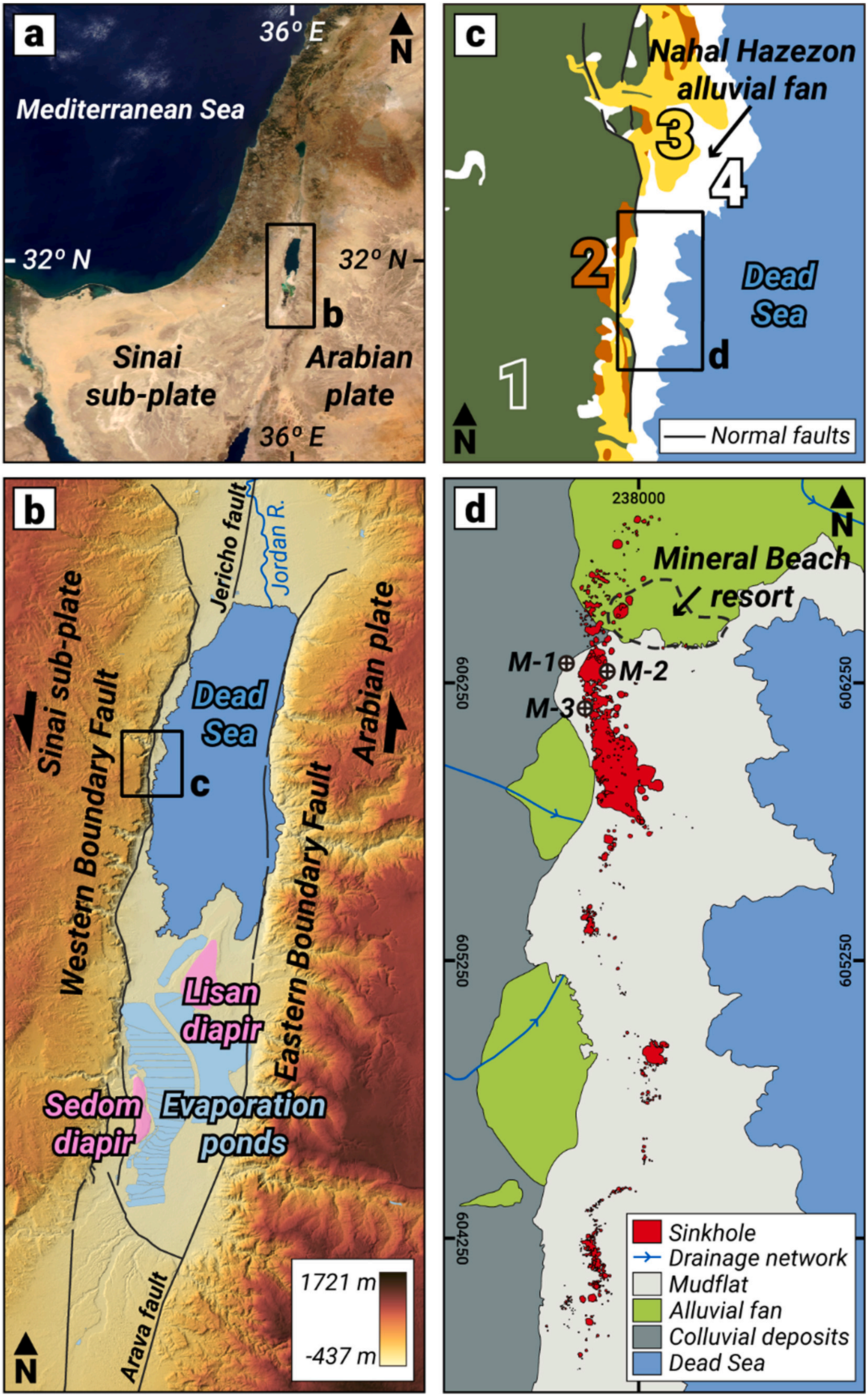

(caption on next page)

Fig. 1. Geological context of the study area. a. Satellite image showing the Dead Sea located in the transform fault system between the Sinai sub-plate and the Arabian plate. b. Topographic model of the Dead Sea area, located in the northern half of a 150-km-long pull-apart basin between the left-stepping Arava and Jericho faults (structural data from Sneh and Weinberger, 2014). Its receding coastline is the lowest land surface in the world (−437 m below sea level according to the Digital Surface Model of 2021 generated for this research). c. Geological sketch of the western sector of the Dead Sea south of the Nahal Hazezon alluvial fan (modified from Mor and Burg, 2000). 1: Upper Cretaceous carbonate units of the Judean Mountains. 2. Pliocene En Feskha conglomerates. 3. Plio-Pleistocene Samra and Lisan Fms. 4. Holocene Ze'elim Fm. d. Geomorphological map of the study area, bounded to the north by the Nahal Hazezon alluvial fan. Morpho-sedimentary units from west to east include colluvial deposits, alluvial fans and mudflats exposed by the decline of the Dead Sea Lake level. The map depicts the 571 sinkholes mapped in the study area in 2021. The dashed line indicates the limits of the abandoned Mineral Beach resort. The location of the three boreholes reported in Yechieli et al. (2006) is shown (M-1 to 3). Coordinate system: EPSG:2039.

with dewatering and compaction of near-surface lake sediments (−24 to −153 mm/year; Vey et al., 2021); (2) large subsidence basins that enclose sinkhole clusters (e.g., Watson et al., 2019); and (3) rapidly forming and evolving collapse sinkholes, which represent the most dramatic and hazardous geomorphic process. The western coast has experienced the formation of >6000 sinkholes since 1980, a process that according to Abelson et al. (2006) displayed an acceleration trend between the 1980s and 2002. Sinkholes have caused substantial damage on human structures (e.g., roads, tourist resorts) and economic activities (potash exploitation, agriculture), and have the potential to cause fatalities (Frumkin and Raz, 2001; Closson and Abou Karaki, 2009a; Frumkin et al., 2011; Abou Karaki et al., 2016, 2019; Nof et al., 2019; Salameh et al., 2019; Vey et al., 2021). Several people have been swallowed by sinkholes formed under their feet (Frumkin et al., 2011). Interestingly, the depressions tend to occur forming clusters along relatively narrow belts away from the shoreline (Abelson et al., 2006; Yechieli et al., 2006; Watson et al., 2019). According to Abelson et al. (2003), the majority of the sinkhole clusters on the western coast display a linear shape with prevalent NE and SSE orientations, coinciding with the principal trends of the exposed faults and the rift wall segments.

Research boreholes that encountered cavities in a shallow Holocene salt unit corroborated the causal relationship between halite dissolution and sinkhole occurrence (Abelson et al., 2006; Yechieli et al., 2006). Two main interpretations have been proposed in the western coast of the Dead Sea to explain the generation of sinkholes within the current lake-level decline context. According to the most widely accepted interpretation, the base-level lowering causes the lakeward migration of the brackish water – saline water interface, allowing undersaturated water to dissolve halite that used to be in contact with saturated saline water (Yechieli et al., 2001, 2006). Different water sources and preferential dissolution zones have been proposed to explain the karstification of the halite unit on the landward side of the brackish-saline water interface (Fig. 2): (1) dissolution at the salt edge by water derived from laterally interfingered alluvial gravels (e.g., Ezersky et al., 2009; Frumkin et al., 2011); (2) dissolution controlled by concealed faults that guide the upward flow of undersaturated water from bedrock aquifers (hypogene karst) (Abelson et al., 2003; Closson, 2005; Shalev et al., 2006); (3) downward percolation of surface water during flash floods via sinkholes that interrupted drainages, functioning as swallow holes (Avni et al., 2016; Arav et al., 2020). An additional interpretation postulates that the lake-level decline is not a requisite for the development of sinkholes, and that halite dissolution can occur on the saline side of the interface by undersaturated groundwater rising from a deep confined aquifer along faults, as supports the presence of sinkholes formed under the lake water (e.g., Frumkin et al., 2011; Closson et al., 2013; Charrach, 2019). All these models are fully compatible and most probably play some role on sinkhole development on the western coast of the Dead Sea, with variable contribution depending on local conditions. On the eastern coast, where the subsurface stratigraphy is poorly known due to the paucity of borehole data, Al-Halbouni et al. (2017, 2021), Polom et al. (2018), and Watson et al. (2019) attribute hectometer-scale subsidence basins with nested collapse sinkholes to the development of solutional conduits in lenticular salt beds and the internal erosion (piping) of detrital deposits. The main differences between the genetic models proposed on the western shore (dissolution model) and the eastern shore (dissolution-piping model) of the Dead Sea are related to the characteristics of the salt deposits and the processes responsible for mass depletion and void creation in the subsurface. All the authors working on the western bank referred to above concur that dissolution of a thick salt layer, regardless of the source of the undersaturated water and the location of the dissolution zone, is the main responsible for sinkhole development (i.e., dissolution model). Conversely, on eastern bank halite is considered to

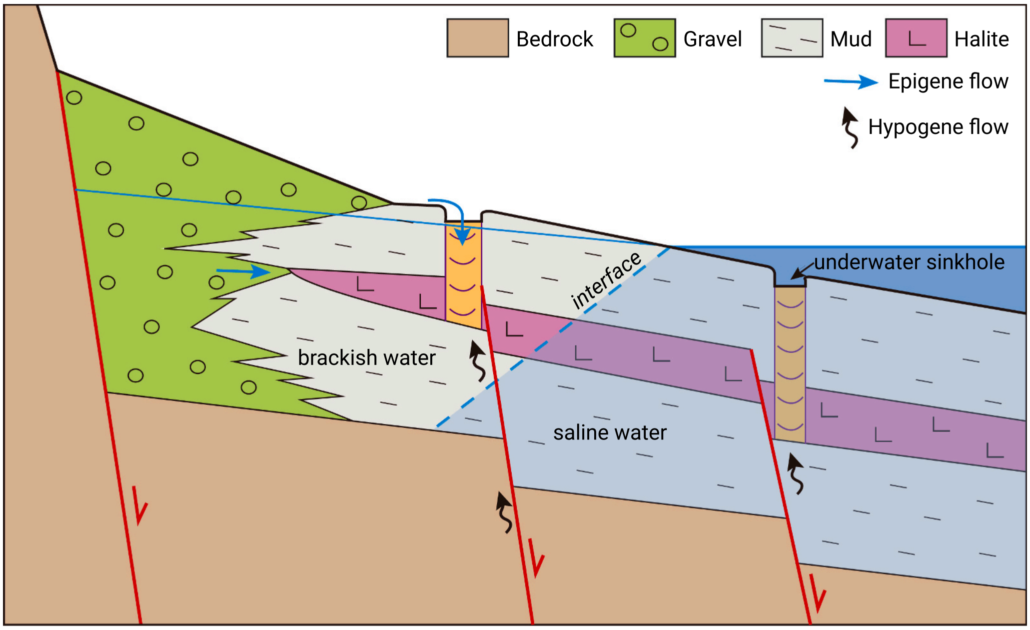

Fig. 2. Conceptual model (not to scale) for the western coast of the Dead Sea showing the two main scenarios in which halite dissolution and sinkhole formation occur, with respect to the lakeward-migrating interface between the brackish and saline water: on the landward side of the interface; and on the lakeward side of the interface, where saturated saline water may be locally diluted by groundwater flows rising from deep aquifers (hypogene flow). Unsaturated water can reach the halite unit from the adjacent gravelly aquifer, by infiltration of surface water via sinkholes, and by rising flows guided by faults from bedrock aquifers.

occur as relatively thin lenticular layers and the subsurface voids responsible for sinkhole development are attributed to salt dissolution and notably to subsurface mechanical erosion (piping) in mud deposits, leading to the development of a dense network of conduits. This dissolution-piping model suggests that the mud deposits are transformed by internal mechanical erosion from an aquitard into a peculiar aquifer of soft muddy sediments with high conduit permeability. According to this model, the evacuation of detrital material from the conduit network occurs via springs with sediment-laden waters observed at the surface, and probably present under the lake waters (Al-Halbouni et al., 2017, 2021; Polom et al., 2018; Watson et al., 2019).

The extraordinary Dead Sea sinkholes have been the subject of a large number of scientific studies. Preliminary maps of sinkhole clusters along the western and eastern shores of the Dead Sea were produced by Frumkin and Raz (2001) and Closson and Abou Karaki (2009b), respectively. Abelson et al. (2006) presented the first multi-temporal inventories of two sinkholes clusters in the western shore of the lake. Besides, sinkhole maps were produced as auxiliary data for detailed geophysical studies on the west (Ezersky et al., 2009; Ezersky and Frumkin, 2020) and east coasts (Al-Halbouni et al., 2021; Ezersky et al., 2021). Filin et al. (2011) conducted the first airborne laser scanning survey of the western shore of the Dead Sea to illustrate the application of the technique to the three-dimensional characterization of sinkholes. Avni et al. (2016) and Arav et al. (2020) used the same method to produce general high-resolution 3D models to assess the relationship between the development of sinkhole swarms and the drainage network at the Ze'elim alluvial fan, the largest one along the Dead Sea coast. Baer et al. (2002), Yechieli et al. (2016) and Nof et al. (2019) applied Interferometric Synthetic Aperture Radar (InSAR) to detect ground deformation in sinkhole sites of the western shore, including slow subsidence preceding collapse. On the eastern shore, Al-Halbouni et al. (2017) and Watson et al. (2019) conducted detailed quantitative analyses of sinkholes and subsidence basins using multi-temporal maps produced with remote-sensed data, including photogrammetric DSMs and orthomosaics. Moreover, Al-Halbouni et al. (2018, 2019) tracked the spatio-temporal evolution of sinkholes to validate geomechanical models of the formation of sinkholes within karstic depressions.

Sinkhole fields evolve over time by various processes: (1) enlargement of pre-existing sinkholes by lateral expansion (surface erosion) and deepening (renewed and continuing subsidence), (2) generation of new sinkholes, and (3) coalescence of two or more sinkholes. The latter process can occur as a consequence of the first two, namely lateral expansion and intersection of pre-existing sinkholes by new ones, and is influenced by spatial factors, such as sinkhole density and clustering, and rheological conditions. While the degree of morphological maturity increases, these processes modify the morphometric and spatial distribution features of the sinkholes. These parameters are critical for the development of sinkhole hazard and risk assessments. However, despite of their practical importance, the evolution of the morphometry and spatio-temporal distribution of sinkholes have been barely explored in real cases (e.g., Festa et al., 2012). This is largely due to the typically slow rates of the geomorphic processes, requiring for their study longer time spans than those covered by the available data. However, the rapidly evolving Dead Sea sinkholes offer an exceptional opportunity for this type of analyses. The main objective of this work is to illustrate such kind of studies using multi-temporal cartographic sinkhole inventories and 3D morphometric data. These data allow analyzing quantitatively a number of evolutionary features with significant geomorphological and practical implications, such as: (1) the role played by sinkhole expansion and coalescence on the morphometric evolution of the depressions; (2) the variable frequency-size relationships of single and compound sinkholes; (3) the impact of clustering versus dispersion on the evolution of sinkholes; (4) the relative distribution between pre-existing and new sinkholes and its utility for sinkhole prediction. The results of the work also provide novel insights into the characteristics and origin of sinkholes and large subsidence basins in the eogenetic salt karst of the Dead Sea.

2. Geological setting

The Dead Sea is a hyper-saline endorheic lake located in the 150-km-long Dead Sea pull-apart basin, with its water level currently lying at ~437 m below sea level (according to the topographic data gathered for this research). The basin formed 18–15 Ma ago between the left-stepping Arava and Jericho strike-slip faults (Fig. 1). These N-trending structures occur in the southern sector of the left-lateral Dead Sea transform fault system, which defines the boundary between the Arabian plate and the Sinai sub-plate. The structure of the Dead Sea basin is controlled by border faults with dominant normal displacement and longitudinal intrabasinal strike-slip faults. It is divided into two main sub-basins separated by the Lisan salt diapir (Fig. 1a and b; Garfunkel and Ben-Avraham, 1996; Abelson et al., 2006; Ben-Avraham et al., 2008).

The sedimentary record reveals that the lake-level has experienced significant variations since the mid-Pliocene as a consequence of climatic fluctuations and the resulting imbalances between water inputs and outputs (Garfunkel and Ben-Avraham, 1996). From that time the northern basin has hosted at least four large paleolakes recorded by the corresponding litho-stratigraphic units: Amora Fm. (220–135 ka), Samra Fm. (135–87 ka), Lisan Fm. (75–14 ka), and Ze'elim Fm. (11 ka–present) (Neugebauer et al., 2014; Coianiz et al., 2019, 2020). There are extensive outcrops of the Lisan Fm. along the Dead Sea coast, which belong to a much larger and deeper late Pleistocene pluvial lake. This formation consists of varves comprising minerals precipitated from the lake water (aragonite, gypsum, and halite), and fine-grained detrital material (Neugebauer et al., 2014; Dor et al., 2019). The younger Ze'elim Fm., inset with respect to the Lisan Fm., is exposed along the rapidly expanding coast. Outcrop and borehole data indicate that its reaches 70 m in thickness and comprises interdigitated alluvial and lacustrine sediments. The latter are characterized by alternating laminae of autochthonous precipitates (aragonite, gypsum, and halite) and mud ascribed to aeolian dust from the Sahara-Arabia deserts (Haliva-Cohen et al., 2012; Neugebauer et al., 2014; Coianiz et al., 2019). According to boreholes drilled in near-shore environments, the lower section of the Ze'elim Fm. is made up of a ca. 10 ka halite unit that was deposited during the transition between the Pleistocene Lisan Lake to the Holocene Dead Sea Lake, during a significant shrinking phase under extremely arid conditions. This porous and poorly lithified salt unit, still in its eogenetic stage, is mainly composed of idiomorphic halite crystals and reaches 25 m in thickness (Yechieli et al., 1993, 1995, 2006; Abelson et al., 2006; Neugebauer et al., 2014).

The study area (Fig. 3a), covering 2.89 km^2, is bounded to the west by the Western Boundary Fault, that essentially juxtaposes Holocene Ze'elim sediments in the downthrown block, against the Quaternary Samra and Lisan formations, underlain by Cretaceous carbonate units of the Judean Mountains (Mor and Burg, 2000; Fig. 1c). From the geomorphological perspective, the analysed piedmont and coastal strip is situated, from north to south, between the southernmost sector of the Nahal Hazezon alluvial fan, and 100 m north of the Ein Kedem North thermal spring. From west to east, the study area comprises the following morpho-sedimentary environments underlain by interdigitated deposits: (1) a strip of relatively steep slopes with colluvial deposits shed from the fault escarpment; (2) alluvial fans fed by the wadis that drain the Judean Mountains, consisting of slightly cemented gravels; (3) mudflats exposed by the anthropogenic decline of the lake level and underlain by soft, laminated lacustrine deposits.

The studied sinkholes mainly occur in the mudflat and, to a lesser extent, in the Nahal Hazezon alluvial fan and the colluvial deposits (Fig. 1d). At the gradational boundary between the Nahal Hazezon alluvial fan and the mudflat there used to be a tourist resort (Mineral Beach), now abandoned as a consequence of its destruction caused by sinkholes (Fig. 3b). The resort was built in an area with a thermal spring with water emerging at around 30 °C. According to borehole data, here

Fig. 3. a. Image of the study area taken from the western escarpment and looking to the north. The Nahal Hazezon alluvial fan is in the background. The arrow points to the location of Mineral Beach resort (shown in b). The mudflat is punctured by sinkhole alignments and numerous coast-parallel linear features (i.e., risers, strand lines) recording previous Dead Sea shorelines. b. Collapse sinkhole affecting the parking lot and some buildings at the Mineral Beach resort. Note the concentric network of cracks beyond the array of boulders, attesting for the substantial expansion of the ground instability phenomenon. The arrow points to a person for scale on the left.

the water rises from deep strata with a salinity of ca. 120 g/L, which is around 35 % of that of the Dead Sea, and hence with high capability to dissolve halite (Abelson et al., 2006; Yechieli et al., 2006). Three boreholes were drilled in the vicinity of Mineral Beach (Yechieli et al., 2006; see Fig. 1d for location). The longest borehole (49 m; M-2 in Fig. 1d) crossed in ascending order: (1) an alternating sequence, 16 m thick, of lacustrine muds and alluvial gravels; (2) a 15-m-thick halite unit between −440 and − 425 m b.s.l.; and (3) a package of 18 m of lacustrine muds. This borehole penetrated a cavity >1.5 m wide at the lower part of the salt unit (between −440 and − 435 m b.s.l.).The muds underlying the halite unit belong to the Lisan Fm., and those above to the Ze'elim Fm. Toward the west, these lake deposits grade laterally through an interdigitated contact into the alluvial fan gravels. This lateral facies change bounds deposits with markedly different permeability and rheology; porous and brittle gravels versus low-permeability and ductile muds. The remaining boreholes, M-1 (35 m) and M-3 (15 m), did not intercept the halite unit, most probably due to the marginal position and limited depth, respectively. The thickness and elevation of the halite unit varies considerably with distance to the lakeshore (Abelson et al., 2006; Yechieli et al., 2006). These variations can be related to the expected pinching-out toward the margin of the basin, truncation and offset of the unit by concealed Holocene faults, and dissolution.

3. Methodology

In order to gain insight into the morphometric and spatio-temporal evolution of the sinkholes in the study area (2.89 km^2), multi-temporal sinkhole maps have been produced covering the period 2005–2021, with intervals of 1–3 years. Sinkhole mapping was conducted in a GIS environment (ArcGIS and QGIS) using various types of imagery: (1) aerial photographs from 2005 to 2011; (2) satellite images from 2015; and (3) orthomosaics produced for this work by Structure from Motion (SfM) Photogrammetry with images taken by a UAV (Unmanned Aerial Vehicle) in 2018 and 2021. We also generated high-resolution photogrammetric digital surface models (DSMs) with the drone images of 2018 and 2021, which were used for measuring planimetric and three-dimensional morphometric parameters of the sinkholes. Table 1 indicates the type of data employed, their source, date, horizontal resolution, and georeferencing error (root mean squared error, RMSE).

For mapping sinkholes within the interval 2005–2011 we produced georeferenced orthomosaics with the corresponding aerial photographs. Initially, we merged the overlapping photographs from each date. Subsequently, we orthorectified and georeferenced the mosaics using between 23 and 29 control points and our SfM-derived 2018 orthomosaic as reference. The control points were restricted to the limited number of persistent locations identifiable on both images. We chose a second order polynomial for georeferencing, which contributes to reduce the influence of the distortion associated with the flight obliquity. All the data sets were georeferenced under the EPSG:2039 coordinate system.

In December 2018 and 2021 we conducted fieldwork in the study area to: (1) check the mapped landforms and identify new ones on the ground; (2) gather data on the sinkhole areas, including outcrops and features not identifiable in the available imagery; and (3) perform drone photogrammetric flights. For the latter task, we installed 30 evenly spaced ground control points (targets 50 cm in diameter) across the study area that were measured with a Differential-GPS (Trimble R8). The drone flights were operated by Terrascan-Labs LTD with a DJI Mavic 2 Pro in 2018 and a DJI Phantom 4 Pro in 2021. We produced high-resolution orthomosaics and digital surface models (DSM) of the vegetation-free surface by SfM Photogrammetry using the software Agisoft Metashape Professional. This photogrammetric approach finds and matches a number of common image features in the overlapping

Table 1
Raster data used for multi-temporal mapping of sinkholes and for characterizing their morphometric features and spatio-temporal evolution. The coordinate system EPSG:2039 was used for all the data sets. RMSE: root mean squared error.

Data type	Source	Date	Elapsed time	Resolution	RMSE
Aerial photographs	Geological Survey of Israel	2005-01-13	–	100 cm/pix	391 cm
Aerial photographs		2006-08-04	1.56 years	95 cm/pix	317 cm
Aerial photographs		2008-12-28	3.96 years	81 cm/pix	337 cm
Aerial photographs		2011-10-11	6.75 years	66 cm/pix	157 cm
Satellite image		2015-09-08	10.66 years	25 cm/pix	124 cm
Drone orthomosaic	Drone images captured by Terrascan-Labs LTD	2018-12-12	13.92 years	4 cm/pix	7 cm
Drone DSM		2018-12-12	13.92 years	15 cm/pix	7 cm
Drone orthomosaic		2021-12-07	16.91 years	4 cm/pix	2 cm
Drone DSM		2021-12-07	16.91 years	17 cm/pix	2 cm

photographs taken for different points, that are subsequently used to establish their exterior and orientation parameters (Micheletti et al., 2015). After assigning coordinates to the 30 ground control points, the software sequentially produced georeferenced high-resolution point clouds, DSMs, and orthomosaics. To maintain consistency between the 2018 and 2021 SfM-derived models, we used the same distribution of GCPs and the same SfM processing parameters.

The multi-temporal sinkhole mapping was carried out by manual digitizing on the various types of imagery. We opted for this method due to the following reasons: (1) the depressions and their boundaries can be confidently identified in the images of the barren and nearly flat ground surface; (2) the approach can be applied to all the dates, allowing the use of consistent mapping criteria; (3) manual mapping involves a thorough virtual examination of the study area, which provides the means for grasping important geomorphic features and relationships that would go unnoticed using automatic methods (Festa et al., 2012; Zumpano et al., 2019; De Waele and Gutiérrez, 2022). Automatic or semi-automatic mapping approaches using DEMs (e.g., Panno and Luman, 2018) were ruled out because they were not feasible for all the dates, and they typically yield a high number of false positive and missed positives (e.g., Wall et al., 2017), as well as imprecise sinkhole boundaries (e.g., Hofierka et al., 2018). Various types of relief models generated with the 2018 and 2021 DSMs (conventional and multidirectional hillshades, Red Relief Image Maps; Chiba et al., 2008; Gökkaya et al., 2021) revealed a tight correspondence between the features mapped with the images and those identifiable in the high-resolution models. In order to track the evolution of the sinkholes (e.g., reactivation, expansion, coalescence) and the occurrence of new ones, we produced maps in chronological order starting with the 2005 images. An identification number was assigned to each sinkhole, that was retained for the following dates. In case of coalescence of two or more sinkholes, the identification number of the larger one was kept for the compound sinkhole. The maps covering the 2005–2021 interval include a total of 935 different sinkholes, of which 702 were newly formed within that time period. The multi-temporal sinkhole database was furnished with attributes such as the morpho-sedimentary environment in which the sinkholes are located (mudflat, alluvial fan, colluvium), whether they were single or compound, and for the sinkholes identified in the high-resolution 2018 and 2021 orthoimages, the subsidence mechanisms (i.e., collapse, sagging, mixed (concurrently or consecutive combination of collapse and sagging processes); Gutiérrez et al., 2008; Gutiérrez, 2016; Parise, 2019). The coastline and the drainage network (gullies), locally interacting with the sinkholes (e.g., blind gullies, dissected sinkholes), were also mapped for each date. Additionally, the two most recent orthoimages, thanks to their high resolution (4 cm), allowed us to identify systems of extensional cracks and scarps developed along the marginal zones of the sinkholes.

The following planimetric morphometric parameters were computed automatically for each sinkhole and each date: major axis, azimuth of the major axis, perimeter, area, circularity ratio, elongation ratio. The three-dimensional parameters, including depth, length-to-depth ratio, and volume were only measured for the sinkholes mapped with the 2018 and 2021 DSMs. Table 2 indicates the definition of the parameters and how they were measured. Sinkhole depth was computed as the elevation difference between the highest point of the edge and the deepest point of the sinkhole. Sinkhole volumes were computed with the SfM-derived DSMs of each sinkhole and their synthetic DEMs, equivalent to their pre-collapse surface, as a pixel-by-pixel volume summation using the Volume Calculation Tool of QGIS (REDcatch GmbH, 2020).

To analyse the spatio-temporal distribution patterns of the sinkholes and the impact of processes such as their areal growth and coalescence, we produce a map for each date assessing the number of sinkholes per hectare. These density maps by number of sinkholes were generated with their centroids and applying a triweight kernel function and a circular search radius of ~56 m (i.e., 1-hectare search area). The percentage of area occupied by sinkholes was measured conducting overlay analyses over an orthogonal mesh with a cell area of 1 ha.

We calculated for every mapped sinkhole the shortest distance between its centroid to the drainage network, its areal expansion with respect to the previous date, and its deepening and volumetric enlargement between sinkholes mapped from 2018 to 2021. We also computed for each date the Nearest Neighbor Index (NNI) (Table 2). The NNI (NNI = La / Le; Clark and Evans, 1954) is the ratio between the average distance between nearest neighbors in the study area (La) and the expected distance between neighbors in a theoretical random distribution with the same distance (Le). It ranges between maximum aggregation (NNI = 0) and maximum dispersion (2.1491). A NNI of 1 means random distribution. We also applied the density-based spatial clustering (DBSCAN; Ester et al., 1996) algorithm to identify clusters among the sinkholes mapped in 2021 (Table 2). It can be applied to group sinkhole centroids that are packed together and mark as outliers the non-clustered ones without indicating the number of clusters in advance, unlike in the widely used k-means clustering method. The low resolution of the initial imagery and the coalescence of sinkholes restricted the assessment of the areal and volumetric evolution of individual sinkholes. We were able to measure the rate of areal change of 71 % of the sinkholes mapped between 2005 and 2021 and the rate of volumetric change of 68 % of the sinkholes mapped from 2018 onwards. The subtle mapping discrepancies related to the different raster resolutions and the georeferencing errors resulted in inaccuracies such as very small negative areal (32 %; median: −0.3 m^2/year) and volumetric (16 %, median: −0.2 m^3/year) change rates.

4. Results

4.1. General features of the sinkholes

A total of 702 new sinkholes have been mapped for the period 2005–2021 (Fig. 4). The multi-temporal cartographic inventories included the differentiation between single and compound depressions, their geomorphic position, and the sinkhole type for those of 2018 and 2021 (collapse, sagging, mixed; Fig. 5). The number of sinkholes mapped in 2005, 2006, 2008, 2015, 2018, and 2021 was 158, 164, 341, 386, 427, 558 and 551, respectively (Fig. 6a). Interestingly, the area covered

Table 2
Parameters measured and calculated from the mapped sinkholes. The table includes its coding, definition, and the procedure followed for obtaining them.

Parameter	Code	Definition	Procedure
Major axis	Ma	Planar length of the straight line between the antipodal points of the sinkhole perimeter	Longest distance between any two vertices of the convex hull that encloses the sinkhole. Convex hull generated using the ArcGIS Minimum Bounding Geometry tool
Azimuth of major axis	AzMa	Orientation of the major axis measured from the North.	Horizontal angle of the major axis (Ma) measured clockwise from the North. Automatically calculated by the ArcGIS Minimum Bounding Geometry tool
Perimeter	P	Length of the mapped sinkhole edge	Measured using R (R Core Team, 2022), the sf package (Pebesma, 2018) and the st_perimeter tool from lwgeom package (Pebesma, 2020)
Area	A	Area enclosed within the perimeter	Measured using R (R Core Team, 2022)and the st_area tool from the sf package (Pebesma, 2018)
Areal change	ΔA	Increase of the area of a sinkhole between, at least, two consecutive dates	(1) Identification of the sinkholes mapped, at least, in two consecutive dates. (2) Area of the sinkholes in the corresponding dates. (3) Time elapsed between the dates of the images used for mapping. (4) Calculation of the rate of areal increase per year. These steps were carried out using R (R Core Team, 2022) and the tidyverse (Wickham et al., 2019), sf (Pebesma, 2018), and data.table (Dowle and Srinivasan, 2022) packages
Circularity ratio	Rc	Ratio between the area of the sinkhole (A) and the area of a circle with the same perimeter as that of the sinkhole (Ap)	$RC = A / Ap$ ($Ap = P^2 / 4\pi$). Computed using R (R Core Team, 2022)
Elongation ratio	Re	Ratio between the diameter (D) of a circle with the same area as that of the sinkhole and the major axis (Schumm, 1956)	$Re = D / Ma$ ($D = 2\sqrt{(A / \pi)}$). Calculated using R (R Core Team, 2022)
Depth	D	Elevation difference between the highest point of the sinkhole edge and the deepest point of the sinkhole	Measured using the QGIS Zonal statistics tool and the SfM-derived DSMs for 2018 and 2021
Length to depth ratio	RMa-D	Ratio between the major axis (Ma) and the depth (Z) of a sinkhole	$RMa\text{-}Z = Ma / D$. Computed using R (R Core Team, 2022)
Maximum deepening rate	ΔD	Maximum deepening rate measured in centimeters per year (cm/year)	(1) Identification of sinkholes mapped in 2018 and 2021. (2) Difference between sinkhole depths in both dates. (3) Calculation of the time elapsed between the dates of the SfM-derived DSMs used for measuring their depth. (4) Calculation of their maximum deepening rate per year. These steps were carried out using R (R Core Team, 2022) and the tidyverse (Wickham et al., 2019) and sf (Pebesma, 2018) packages
Volume	V	Summation of the pixel-by-pixel volumes within the sinkhole perimeter bounded between synthetic DEMs (pre-collapse surface) and the SfM-derived DSM (sinkhole topography)	Addition of the pixel-by-pixel volumes of all the raster cells within the sinkhole perimeters between their synthetic DEMs and the SfM-derived DSM of 2018 and 2021. Estimated using the QGIS Volume Calculation Tool (REDcatch GmbH, 2020)
Volumetric change	ΔV	Increment of the volume of a sinkhole between 2018 and 2021	(1) Identification of distinctive sinkholes mapped in the 2018 and 2021 images. (2) Sinkhole volume in each date. (3) Calculation of the time elapsed between the dates of the SfM-derived orthomosaics used for mapping. (4) Calculation of the annual rate of volumetric change. These steps were carried out using R (R Core Team, 2022) and the tidyverse (Wickham et al., 2019), sf (Pebesma, 2018), and data.table (Dowle and Srinivasan, 2022) packages
Shortest distance between sinkhole centroid and drainage network	SD-sinkhole drainage	Distance between the centroid of a sinkhole and the closest drainage (gully) in the corresponding date	Measured using R (R Core Team, 2022), the tidyverse package (Wickham et al., 2019) and the st_distance tool from the sf package (Pebesma, 2018).
Nearest Neighbor Index	NNI	Assessment of the degree of clustering versus dispersion by the ratio between the average distance between nearest sinkholes (centroids) in the study area and the expected distance between sinkholes with a theoretical	Calculated using R (R Core Team, 2022) and the nni tool (envelope as minimum bounding geometry) from the spatialEco package (Evans and Murphy, 2021)

(continued on next page)

Table 2 (*continued*)

Parameter	Code	Definition	Procedure
		random distribution and the same density (Clark and Evans, 1954)	
Density-Based Spatial Clustering of Application with Noise	DBSCAN	Density-based assessment of point clustering. Sinkhole centroids in this case.	Calculated using the algorithm proposed by Ester et al. (1996), the nearest neighbor graph created by the dbscan (Hahsler et al., 2019) package, and the QGIS DBSCAN clustering tool. We considered a threshold of 3 sinkholes for a region to be considered dense and a maximum grouping distance of 55 m between points calculated with a nearest neighbor graph of the sinkholes mapped in 2021

by sinkholes shows a steady increase from 1 to 4 % of the study area (Fig. 6c), whereas the increasing trend of the number of sinkholes reverses between 2018 and 2021, despite the significant improvement of the resolution of the images from 2018. This pattern is related to both the coalescence of sinkholes and the expansion of the depressions by mass wasting processes, entailing a decrease in the number of sinkholes and an increase in the area covered by them. The 551 sinkholes mapped with the 2021 high-resolution orthoimages and DSM comprised: (1) 473 single and 78 compound depressions; (2) 469, 62 and 20 sinkholes located in the mudflat, the alluvial fans and colluvial deposits, respectively; and (3) 404 collapse sinkholes, 90 sagging sinkholes, and 57 mixed sinkholes (Figs. 4, 5).

As displayed in Fig. 4, the 2021 sinkholes are concentrated along a narrow strip with a general N-S orientation lying between the Dead Sea Western Boundary Fault escarpment and the receding coastline. The strip comprises a number of sinkhole alignments and strongly elongated clusters with sharp changes in orientation, ranging from NNW-SSE to NE-SW. In 2021, the sinkhole density in the study area (2.89 km^2) was 191 sinkholes/km^2. However, due to the highly clustered distribution of the sinkholes along a well-defined belt, they can be enclosed by a single convex hull polygon (i.e., polygon of minimum perimeter containing all the sinkholes) 3087 m long and 454 m wide that occupies an area of 1.13 km^2. The density of sinkholes considering this minimum bounding geometry rises to 488 sinkholes/km^2. These are exceptionally high densities compared with those reported in other sinkhole areas worldwide (see table and references in De Waele and Gutiérrez, 2022, p. 431). The cumulative area of the 2021 sinkholes, excluding nested ones, is 0.11 km^2, yielding percentage areal densities of 4 % and 10 % with respect to the whole study area and the convex hull polygon, respectively. The graphs in Fig. 6 show the temporal evolution of the number of sinkholes partitioned by their geomorphic setting, differentiating between single and compound, and considering the subsidence mechanism (for 2018 and 2021). The sinkholes mapped in 2006 are not indicated because of the lack of data in the southernmost area (Fig. 4). The great majority of the sinkholes were single and developed in the mudflat, which occupies 65 % of the study area. However, mixed

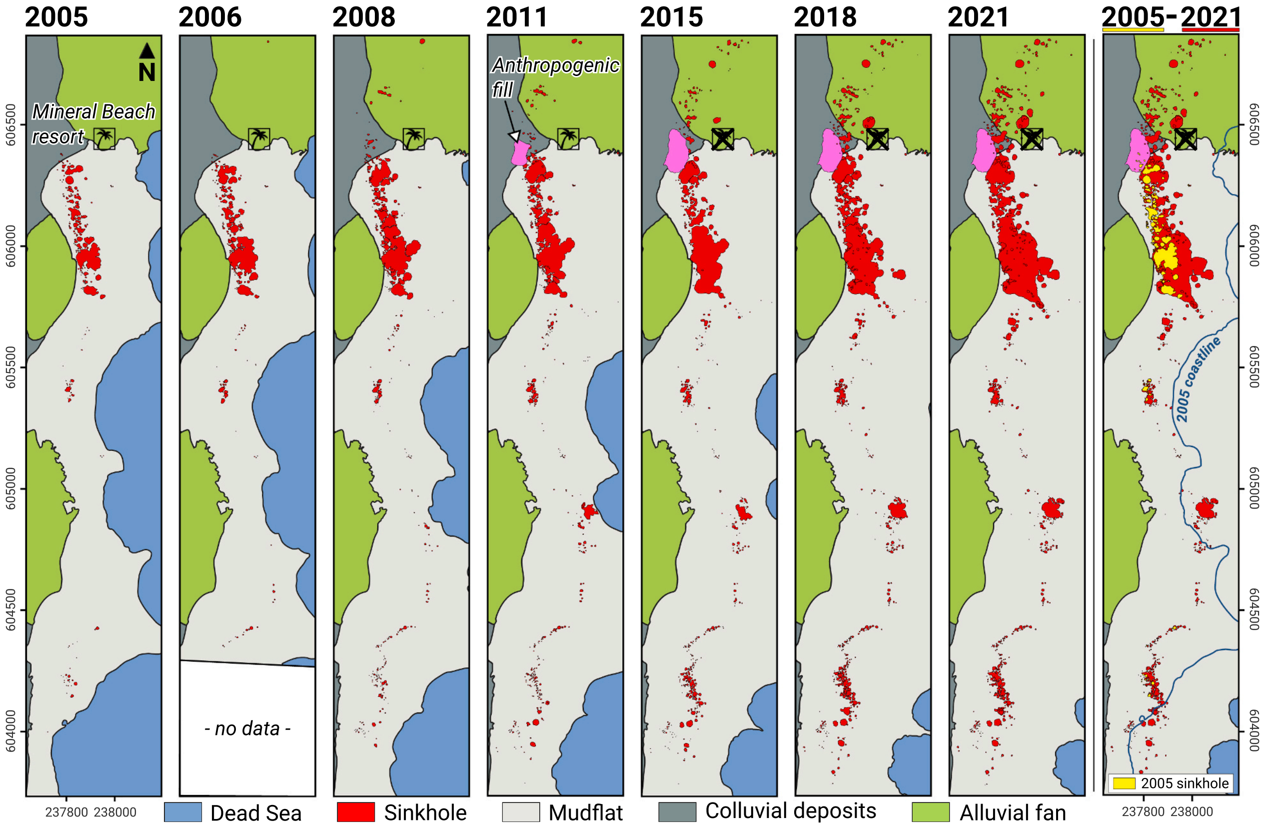

Fig. 4. Evolution of the spatial distribution of sinkholes between 2005 and 2021. The sequence of maps shows the enlargement of the emerged land and the increasing area occupied by sinkholes related to the formation of new ones, the expansion of depressions by mass wasting processes, and their coalescence. Note the longitudinal and lakeward expansion of the linear sinkhole clusters and the formation of new ones, progressively filling the gaps along a well-defined sinkhole belt. The location of the Mineral Beach resort is indicated, closed in 2015 because of its destruction by sinkholes. The maps also show the anthropogenic fill dumped in the study area between 2008 and 2011 and its enlargement. It covered pre-existing sinkholes, some of which punctured its eastern sector between 2015 and 2018.

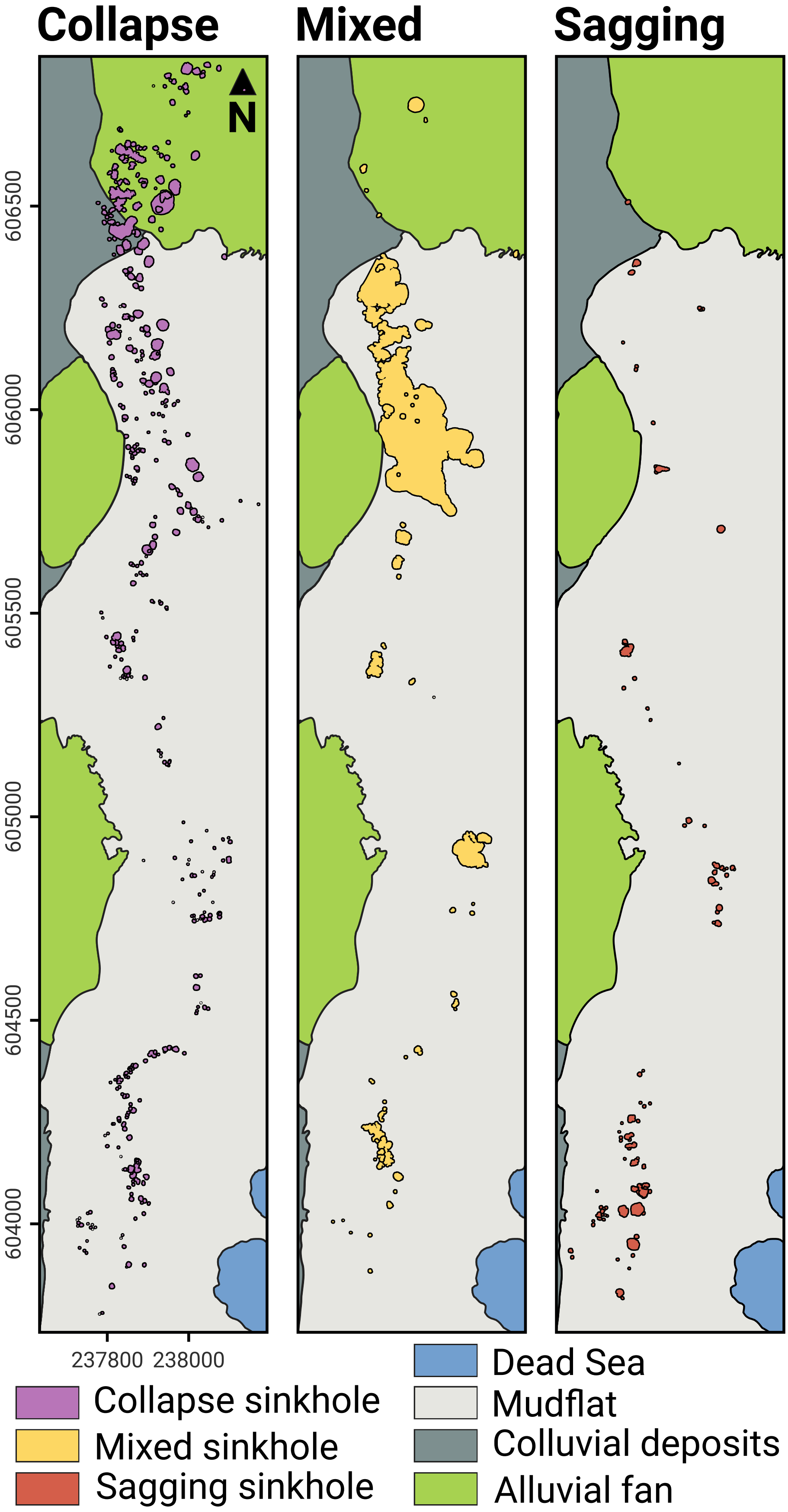

Fig. 5. Spatial distribution of the 2021 sinkholes in the different geomorphic units grouped by the main subsidence mechanisms inferred from their surface expression. Note that sagging sinkholes are essentially restricted to the mudflats underlain by ductile deposits. These sinkholes typically evolve into collapse or mixed (sagging and collapse) sinkholes.

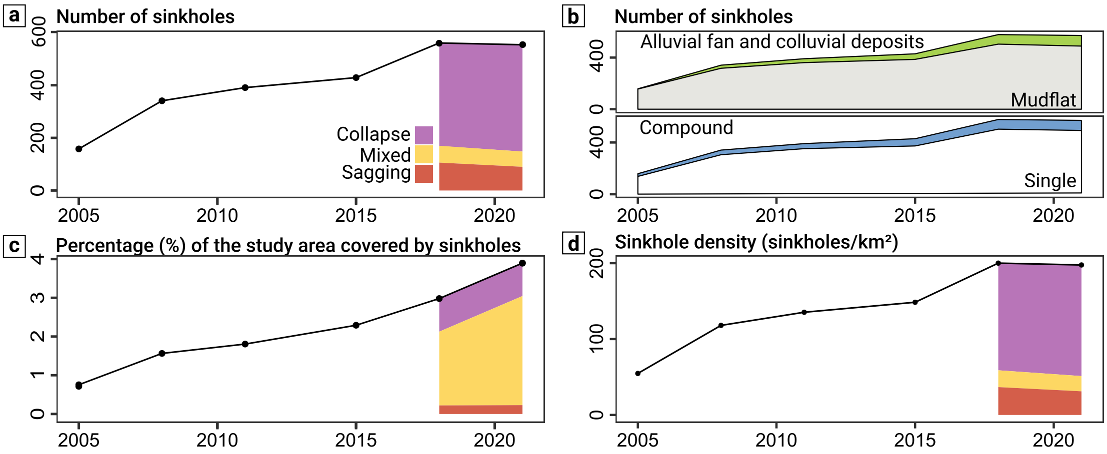

Fig. 6. Graphs showing some features related to the temporal evolution of sinkholes in the study area. The sinkholes mapped in 2006 are not indicated due to the lack of data in the southernmost sector of the study area. a. Number of sinkholes from 2005 to 2021 indicating the share of the different subsidence mechanisms for 2018 and 2021. b. Number of sinkholes mapped for each year partitioned according to the geomorphic unit, and whether they are single or compound. c. Temporal evolution of the sinkhole density expressed by percentage area occupied by sinkholes. d. Temporal evolution of the sinkhole density by number of sinkholes. Note the decrease in the number of sinkholes and sinkhole density by number between 2018 and 2021.

sinkholes account for the highest percentage of the area occupied by sinkholes due to their larger dimensions (Figs. 5, 6c). Like the number of sinkholes, the sinkhole density by number shows a decrease between 2018 and 2021 related to both the coalescence and expansion of the strongly clustered sinkholes (Fig. 6a, d).

We examined the sinkholes during field campaigns conducted in 2018 and 2021 (Fig. 7). Overall, the collapse sinkholes displayed well-defined scarped edges in the mudflat and in the alluvial and colluvial deposits (Fig. 7a, b), unlike the sagging sinkholes, characterized by vaguely defined boundaries expressed as gentle flexures, fissures and scarplets (Fig. 7c, d). The margins of the collapse sinkholes in the gravelly alluvial fan and colluvial deposits are frequently affected by falls and topples controlled by unloading cracks, leading to the accumulation of debris at the foot of the scarp (Fig. 7b). The margins of the collapse sinkholes in the mudflat are mostly affected by rotational slides (Fig. 7e) and less frequently topples (Fig. 7f). The slumps locally show significant retrogressive progression, resulting in the rapid enlargement of the collapse sinkholes in the mudflat by mass wasting, rather than dissolution-induced subsidence. Sagging sinkholes often contain nested collapse sinkholes (Fig. 7d) and some of them evolved into collapse sinkholes between 2018 and 2021 (Fig. 7c). The mixed sinkholes, the least frequent ones, share morphological characteristics of collapse and sagging sinkholes (Fig. 7g). In some areas, the coalescence of tightly packed sinkholes has generated compound depressions that may exhibit a hummocky topography where it is difficult to differentiate the primitive sinkholes (Fig. 7i). The process of sinkhole coalescence can be related to the expansion of adjoining sinkholes, and to the occurrence of new ones intersecting pre-existing nearby sinkholes. In the southern sector of the study area, the sinkholes are distributed along narrow N-S and NE-SW alignments in the mudflat with an en echelon pattern (Figs. 4, 7j).

Between 2018 and 2021, the study area experienced remarkable geomorphic changes, mainly including the occurrence of new sinkholes and the enlargement and coalescence of previous ones (Fig. 8). For instance, in the parking lot of Mineral Beach resort, lying on the Nahal Hazezon alluvial fan, two decameter-scale and one meter-scale collapse sinkhole appeared. Moreover, the concentric cracks of a large pre-existing collapse sinkhole located at the center of the parking lot expanded, especially toward one of the new collapse sinkholes to the north (Fig. 8a, a′). In the alluvial fan, pre-existing collapse sinkholes experienced enlargement by mass wasting acting on their margins and/or renewed subsidence, and new collapse sinkholes formed without any visible precursory sign in 2018 (Fig. 8b, b′). In the mudflat, the largest compound depression of the study area experienced the greatest changes on its southeastern sector. Three large collapse sinkholes formed in between two compound sinkholes, merging into a larger compound depression (Fig. 8c, c′). This is an example of coalescence through the occurrence of new sinkholes. Interestingly, in 2018 there was a precursory gentle sagging sinkhole with marginal cracks at the site where one of the new collapse sinkholes formed (Fig. 7c and yellow arrow in Fig. 8c). Some areas with clustered sinkholes were affected by the formation of new isolated sinkholes, the occurrence of sinkholes nested into pre-existing ones, and the coalescence of depressions by the expansion of their boundaries and/or the occurrence of new intervening ones (Fig. 8d, d′). In some areas sinkholes disrupt pre-existing gullies, eventually acting as ponors (i.e., swallow holes). Fig. 8e, e′ illustrates that between 2018 and 2021 a compound sinkhole intercepting two gullies expanded and was connected to the nearby single sinkhole by a deep and narrow channel. In this sector a new collapse sinkhole occurred over this time lapse but it was separated from both the gullies and the sinkhole cluster.

Around 80 % of the 551 sinkholes of the 2021 inventory are located within 10 subsidence basins up to 1174 m long and 251 m across defined by concentric fissures and inward-facing scarps recognizable in the high-resolution orthomosaics and DSMs produced with the drone images. These surface ruptures are associated with gentle flexures, being more conspicuous on the eastern flank where the monoclines face upslope locally reversing the surface gradient. The opening, throw and lateral continuity of these ruptures tend to be greatest along the crest of the flexures and decrease outward (Fig. 9a′–e′). The lower part of the monoclinal slopes locally shows pressure ridges up to several decimeters high, attributable to contraction in the inner/upper arc of the lower flexures of the monoclines (Fig. 7h). Similar landforms have been described in active subsidence basins related to natural and human-induced dissolution of Triassic salt in the UK (Serridge and Cooper, 2022).

In addition to the sinkholes related to salt dissolution, we identified 20 small collapses in 2021 attributable to shallow subsurface mechanical erosion (i.e., piping; Bernatek-Jakiel and Poesen, 2018). These depressions are much smaller than the mapped sinkholes, are mostly associated with gullies carved in the mudflat, and tend to grow in the direction of the slope gradient, eventually exposing shallow conduits as small natural bridges (Fig. 10). The median values of the major axis, perimeter, area, depth, and volume of the mapped pipe collapses are 2.1 m, 5.8 m, 2.4 m^2, 0.3, and 0.1 m^3, respectively.

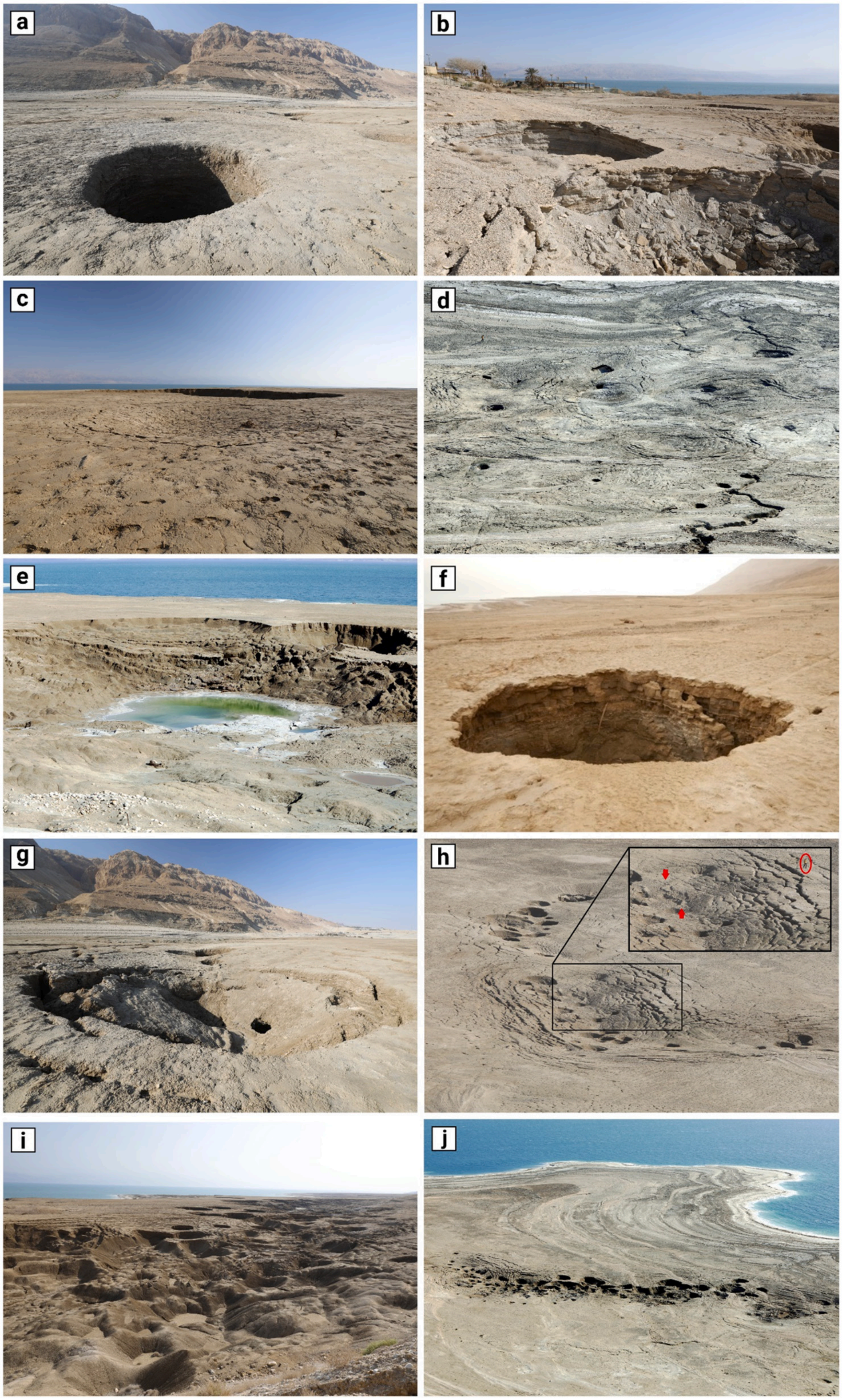

Fig. 7. Images of sinkholes taken in 2018 and 2021. a. Collapse sinkhole on the mudflat showing high circularity and a well-defined scarped edge. b. Collapse sinkholes on the alluvial fan next to the abandoned Mineral Beach resort (left background of the image). Note debris shed from the sinkhole scarp by falls and topples consisting of slightly cemented gravels. c. Shallow meter-scale sagging sinkhole with a marginal concentric network of cracks. It evolved into a decameter-scale collapse sinkhole between 2018 and 2021 (Fig. 8c and c′). d. Cluster of sagging sinkholes bounded by concentric cracks and punctured by nested collapse sinkholes. e. Eastern scarp of a compound sinkhole developed on the mudflat. Note retrogressive rotational slides (slumps) associated with the sinkhole margin responsible for the expansion of the depression by mass wasting. f. Collapse sinkhole in the mudflat with an incipient topple at its scarped margin. g. Mixed sinkhole in the mudflat. h. Large subsidence depression in the southern sector of the study area. The red arrows point to a decimeter-scale pressure ridge formed in its lower sector. Person for scale. i. Image of the largest compound sinkhole of the study area with hundreds of coalesced and nested sinkholes separated by rounded ridges forming a rough hummocky topography. j. Hectometer-scale elongated sinkhole cluster in the mudflat formed by tightly packed individual and compound sinkholes. This lineament follows a NNW-SSE orientation roughly parallel to the Dead Sea Western Boundary Fault.

4.2. Morphometric characteristics and their evolution

The mapped sinkholes show a wide range of dimensions and their main morphometric parameters (i.e., major axis, perimeter, area, depth, and volume) display a highly right-skewed distribution over a wide range of sizes, meaning many sinkholes with relatively small sizes and few with very large ones. To describe the morphometric data, we prefer using statistical values that are robust for skewed distributions, such as the median over the mean, as a measure of the central value of the size distribution, and the interquartile range (IQR) over the range, as a measure of the statistical dispersion. Nonetheless, we have also included the widely used mean values and the range for comparison with other sinkhole studies.

The morphometric parameters of the sinkholes mapped in 2021

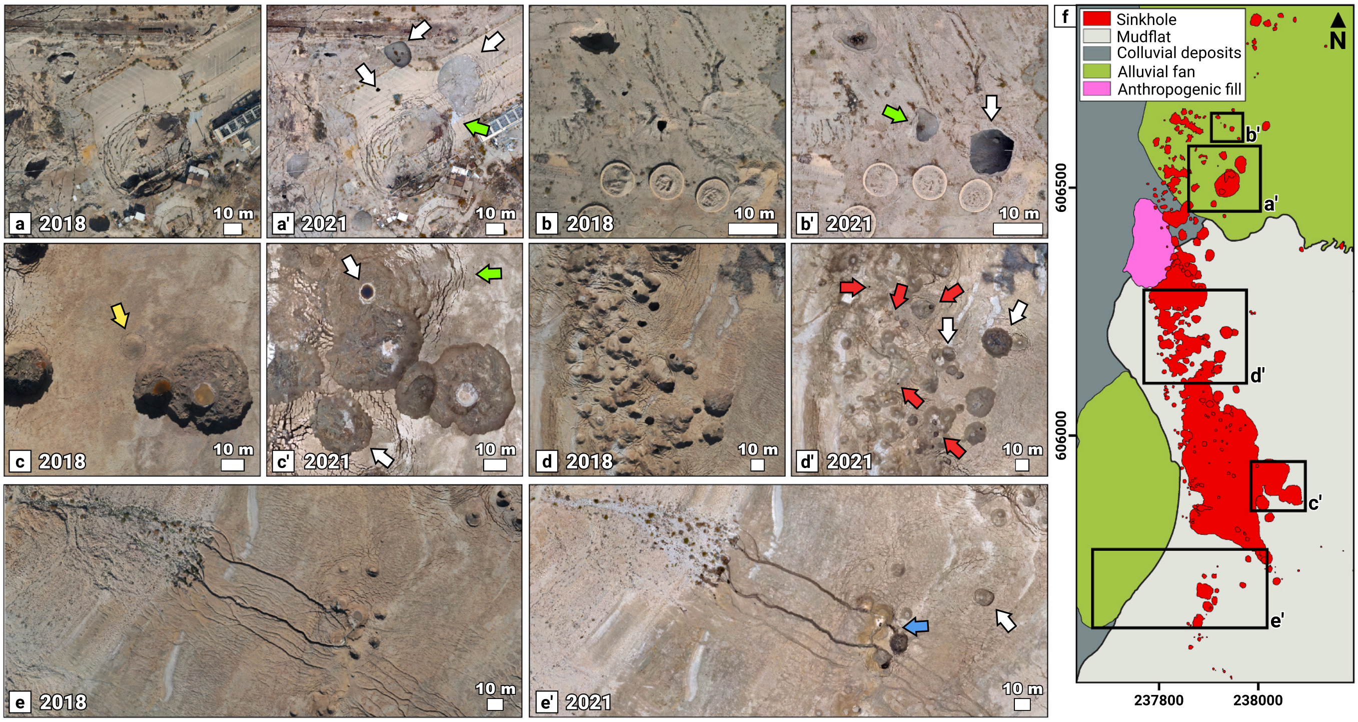

Fig. 8. Images captured from the SfM-derived orthomosaics showing the evolution of five zones between 2018 (a–e) and 2021 (a′–e′). See text for description. White arrows point to new sinkholes formed between 2018 and 2021. Green arrows indicate sinkholes that experienced significant expansion by mass wasting processes (i.e., slumps, falls, topples). Red arrows point to newly formed nested sinkholes. Blue arrow indicates a new gully section connecting two adjacent sinkholes. f. Location of the five zones in the 2021 map.

show median values of 6.1 m, 17.6 m, and 22.7 m^2 for the major axis length, perimeter, and area (Table 3), as well as 1.5 m and 6.8 m^3 for the depth and volume (Table 4), respectively. Over the entire investigation time, the major axis, perimeter, area, depth, and volume of the sinkholes showed similar median, IQR, and minimum values (Tables 3 and 4). However, their maximum values increased every year as a consequence of the enlargement of pre-existing sinkholes. The median annual areal expansion of single sinkholes between successive years ranged between 0.7 and 2.1 m^2/year (overall median: 1.0 m^2/year), representing annual areal increments of 5.7 to 16.4 %, respectively. These values provide a measure of the impact of mass wasting processes in the areal growth of sinkholes; on average, single sinkholes experienced an 8.6 % areal increase over ten years (i.e., 2008–2018). We tested the relationship between the rate of areal enlargement of the sinkholes between 2018 and 2021, and their shortest distance from their centroids to any gully (i.e., proximity). We found a weak (Spearman's rho = 0.31) and statistically significant (p-value = 7.151E-10) positive correlation between them suggesting that there is not a strong linear correlation between those variables. This means that the sinkholes that grew faster were not necessarily the ones that were in the vicinity of the gullies. However, rapid enlargement in the sinkholes that intercept gullies could be expected during flash floods; as described by some authors (e.g., Avni et al., 2016; Arav et al., 2020).

The aggregated area of all the sinkholes mapped in 2021, excluding the nested sinkholes to avoid double-counting the same area (i.e., spatial redundancy), is 112,482 m^2. From 2005 to 2021, the total area covered by sinkholes increased on average 5362 m^2/year. Theoretically, expanding single sinkholes are expected to enlarge at progressively higher rates as their perimeter increases, whereas the available space for the areal growth of sinkholes before their coalescence decreases due to competition for space in areas with clustered distribution (De Waele and Gutiérrez, 2022). However, from 2005 to 2021 the median areal expansion rates of single sinkholes showed low variability, ranging between 1.1 (2008) and 0.7 m^2/year (2015) (Table 3). Most of the sinkholes from 2005 to 2021 were dominantly subcircular, as shown by the computed circularity and elongation ratios (Table 3). The azimuth of the major axes of the elongated sinkholes (i.e., elongation ratio ≤ 0.82 or major axis to width ratio of ≥1.2) displays a wide distribution, with a weak prevalence between 45 and 135°, roughly perpendicular to the main trend of the sinkhole alignments (Fig. 11).

The maximum sinkhole depth in 2021 is 21.2 m, corresponding to the largest compound sinkhole (Fig. 7g). However, in general, the sinkholes are relatively shallow (median depth of 1.4 and 1.5 m in 2018 and 2021, respectively). The median of the deepening rates calculated with the deepest points of the sinkholes in 2018 and 2021 was 5.9 cm/year. This value indicates that sinkholes grew not only by lateral expansion, but also by deepening related to internal subsidence. The fastest deepening rate of 2 m/year was measured in the largest compound sinkhole of the study area. The wide range of the length-to-depth ratio, spanning between 1.1 and 28.9, reflects the broad 3D morphological spectrum between pan-shaped and shaft-like sinkholes. However, the median values of 2018 and 2021 (4.9 and 4.4, respectively) indicate a prevalence of intermediate morphologies between the aforementioned profiles. The median volume computed for 2021 is 6.8 m^3, and the maximum volume 228,343 m^3, measured in the largest compound sinkhole. The aggregate volume of all the sinkholes mapped in 2021 is 329,148 m^3. To avoid double-counting the volume of nested sinkholes, the sum was conducted merging the sinkholes and their nested collapses. The median of the volumetric change of single sinkholes between 2018 and 2021 was 0.3 m^3/year, which represents an annual enlargement of 9 %. The total volumetric change between 2018 and 2021 was 151,792 m^3, yielding an average subsidence rate in the study area of 45 cm/year considering the aggregated area of all the sinkholes mapped in 2021 (112,482 m^2). This value accounts for ground subsidence related to both dissolution-induced subsidence of previous and new sinkholes.

The morphometric parameters of the sinkholes over the analysed period were significantly different (minimum p-value equal to 0.004 for

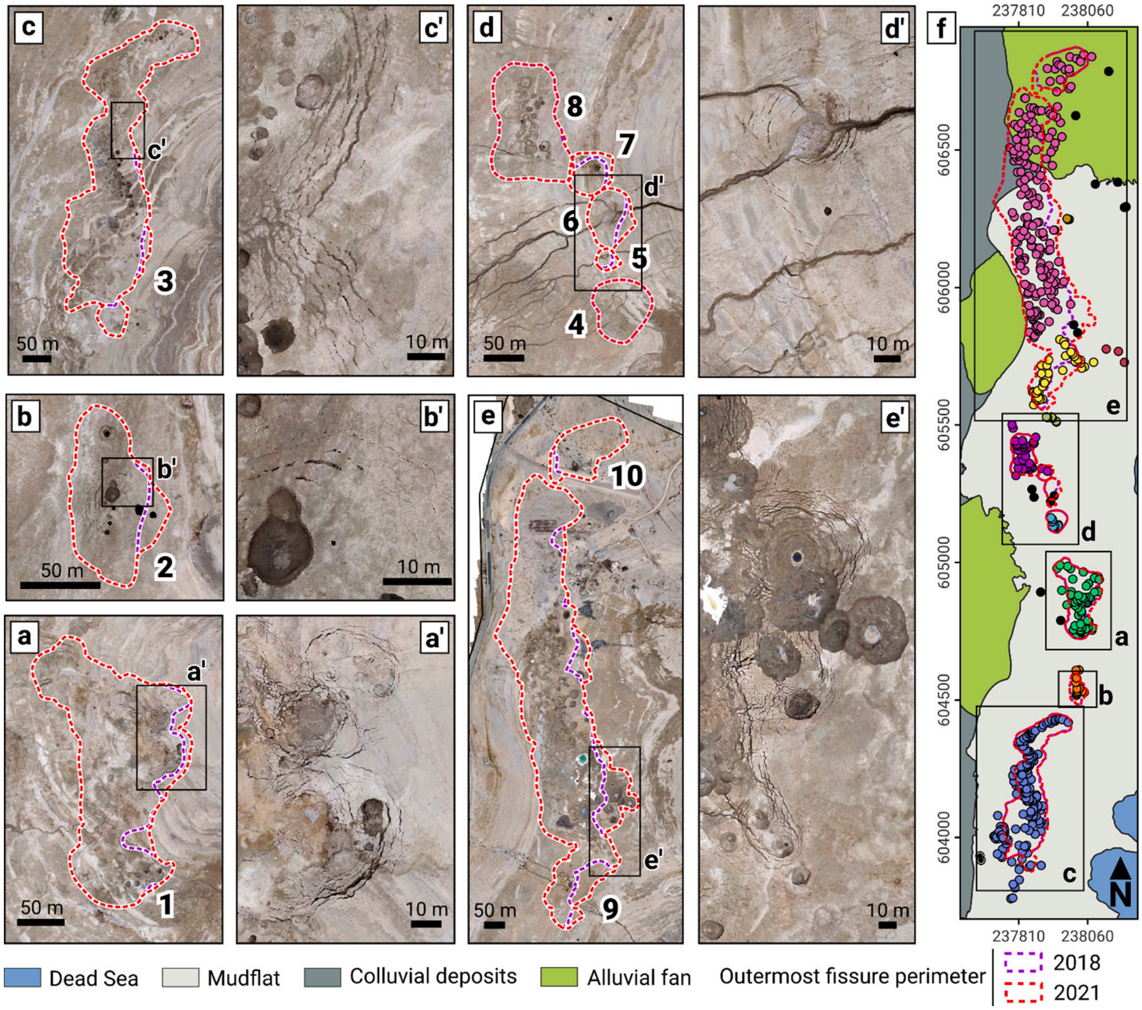

Fig. 9. Large subsidence basins defined by concentric fissures and scarps enclosing sinkhole clusters. a–e. Shots of the 2021 orthomosaic centered on the clusters identified by the DBSCAN algorithm, each labelled with a number. Note the general eastwards (lakeward) expansion of the subsidence basins between 2018 and 2021. a′–e′. Close-up views of the 2021 orthomosaic in which it is possible to recognize the peripheral sets of fissures and scarps. f. Clustering analysis conducted with the DBSCAN algorithm (Ester et al., 1996) with the centroids of the sinkholes mapped in 2021. The colors indicate the different clusters and the black dots outliers (non-clustered sinkholes according to the DBSCAN algorithm). The map also shows the perimeters of the large subsidence basins in 2018 and 2021.

Fig. 10. Images of pipe collapses associated with gullies carved in the mudflat. a. Capture of the 2021 orthomosaic showing a cluster of small pipe collapses associated with gullies. b. View of a pipe collapse intercepting a gully, suggesting the development of a pipe beneath the gully (see (a) for location). c. View of an elongated collapse depression connected to the termination of a gully with a natural bridge in between (unroofed pipe) (see (a) for location).

the comparison between medians - Mood's Median Test) depending on whether they were single or compound sinkholes, on the geomorphic units in which they developed (alluvial fan and colluvial deposits, or mudflat), and on the subsidence mechanism (collapse, sagging, or mixed). Table 5 provides summary statistics of the morphometric parameters of the sinkholes mapped in 2021 differentiating their evolutionary type (single or compound), their morpho-sedimentary environment and their type. As expected, compound sinkholes are larger than the single ones, with higher median values for the major axis, perimeter, area, depth, and volume. The comparison of the compound and single sinkholes reveals that the process of coalescence tends to increase the elongation and length-to-depth ratio and decrease the

Table 3
Morphometric parameters of the sinkholes mapped over the interval 2005–2021. The table shows the number of sinkholes mapped each year (N) and the summary statistics of the planimetric morphometric parameters. The 'unknown' areal change value indicates the number of sinkholes for which the parameter could not be measured or provided an erroneous value because of (1) insufficient resolution of the data, (2) georeferencing errors, or (3) the evolution of the sinkholes themselves related to processes such as their occurrence and coalescence (see Methodology for further clarification).

	2005, N = 158	2006, N = 164	2008, N = 341	2011, N = 386	2015, N = 427	2018, N = 558	2021, N = 551
Major axis length (m)							
Median (IQR)	5.2 (3.3–11.1)	5.9 (4.0–10.7)	4.7 (3.1–8.4)	4.9 (3.4–8.2)	5.2 (3.3–9.2)	5.8 (3.5–9.9)	6.1 (3.9–11.0)
Mean (range)	10.1 (1.0–122.8)	10.9 (1.0–158.1)	8.9 (1.0–206.5)	8.8 (1.3–241.5)	9.5 (0.6–328.8)	9.8 (0.7–330.1)	10.8 (0.9–437.1)
Perimeter (m)							
Median (IQR)	14.6 (9.5–32.1)	16.1 (11.5–29.7)	13.2 (8.6–23.6)	13.7 (9.6–22.6)	15.0 (9.3–25.8)	16.2 (10.1–27.8)	17.6 (11.1–32.0)
Mean (range)	29.9 (2.8–526.2)	33.0 (2.8–707.9)	25.9 (2.8–849.8)	26.3 (3.7–1093.3)	28.2 (1.7–1073.5)	29.8 (1.9–1200.8)	33.5 (2.5–1649.2)
Area (m^2)							
Median (IQR)	16.0 (6.8–64.9)	19.9 (10.0–63.4)	13.2 (5.6–35.1)	13.7 (7.0–35.0)	16.2 (6.6–45.8)	19.4 (7.6–52.7)	22.7 (8.8–65.9)
Mean (range)	137.9 (0.6–7237.3)	180.1 (0.6–11,351.7)	132.5 (0.6–14,239.6)	135.1 (1.0–19,974.6)	155.0 (0.2–29,211.9)	157.8 (0.3–32,682.7)	210.3 (0.5–50,410.0)
Areal change of single sinkholes (m^2/year)							
Median (IQR) [Δ%/year]		2.1 (0.4–6.4) [16.4]	1.1 (0.5–2.9) [6.5]	1.2 (0.5–2.3) [11.1]	0.7 (0.3–1.7) [5.7]	1.1 (0.5–2.9) [8.9]	0.9 (0.4–2.2) [5.7]
Mean (range)		5.5 (0.0–71.5)	5.5 (0.0–141.6)	3.7 (0.0–169.5)	2.5 (0.0–39.5)	3.1 (0.0–75.5)	2.5 (0.0–100.0)
Unknown		55	218	163	253	177	103
Circularity ratio							
Median (IQR)	1.0 (0.9–1.0)	1.0 (0.9–1.0)	1.0 (0.9–1.0)	0.9 (0.9–1.0)	0.9 (0.9–1.0)	0.9 (0.9–1.0)	0.9 (0.8–1.0)
Mean (range)	0.9 (0.3–1.0)	0.9 (0.3–1.0)	0.9 (0.2–1.0)	0.9 (0.2–1.0)	0.9 (0.2–1.0)	0.9 (0.2–1.0)	0.9 (0.2–1.0)
Elongation ratio							
Median (IQR)	0.9 (0.8–0.9)	0.9 (0.8–0.9)	0.9 (0.8–0.9)	0.9 (0.8–0.9)	0.9 (0.8–0.9)	0.9 (0.8–0.9)	0.9 (0.8–0.9)
Mean (range)	0.8 (0.6–1.0)	0.9 (0.6–1.0)	0.9 (0.5–1.0)	0.8 (0.6–1.0)	0.9 (0.5–1.0)	0.9 (0.5–1.0)	0.8 (0.5–1.0)

Table 4
Summary statistics of the three-dimensional morphometric parameters of the sinkholes mapped for 2018 and 2021. The 'unknown' deepening and volumetric change values indicate the number of sinkholes for which these parameters could not be measured or provided a negative value because of (1) insufficient resolution of the data, (2) georeferencing errors, or (3) the evolution of the sinkholes themselves, involving processes such as their occurrence and coalescence (see Methodology for further clarification).

	2018, N = 558	2021, N = 551
Depth (m)		
Median (IQR)	1.4 (0.6–2.6)	1.5 (0.8–3.0)
Mean (range)	2.0 (0.0–5.1)	2.3 (0.1–21.2)
Length to depth ratio		
Median (IQR)	4.9 (3.5–7.2)	4.4 (3.3–6.1)
Mean (range)	5.8 (1.2–49.1)	5.2 (1.1–28.9)
Deepening rate (cm/year)		
Median (IQR)		5.9 (3.3–10.2)
Mean (range)		10.7 (0.1–202.5)
Unknown		193
Volume (m^3)		
Median (IQR)	5.5 (0.7–33.8)	6.8 (1.0–41.4)
Mean (range)	321.0 (0.0–103,626.0)	605.4 (0.0–228,342.6)
Volumetric change of single sinkholes (m^3/year)		
Median (IQR) [Δ%/year]		0.3 (0.1–1.3) [9.1]
Mean (range)		4.5 (0.0–468.3)
Unknown		151

circularity of the depressions. Between 2018 and 2021, the compound sinkholes showed higher rates of areal expansion, deepening, and volumetric enlargement than the single sinkholes. The maximum volumetric sinkhole growth rate (41,686 m^3/year) was mainly related to the coalescence of two adjoining compound depressions as a consequence of the occurrence of new intersecting sinkholes in between (Fig. 7c–c′). However, the percentage areal and volumetric growth rates were higher for the single sinkholes, meaning that the compound sinkholes experienced a slower relative growth (Table 5).

Regarding the geomorphic units on which they occur, the median of the major axis, perimeter, area, depth, and volume of the sinkholes in the alluvial fan and colluvial deposits are larger than those in the mudflat. However, there are many compound sinkholes in the mudflat that are much larger than the compound sinkholes in the alluvial and colluvial deposits. The median of the length-to-depth ratios shows similar values for the sinkholes developed in the alluvial fan and colluvial deposits (3.4) and in the mudflat (4.6). It also shows that the pan-shaped sinkholes (i.e., high length-to-depth ratio) are distinctly typical of the mudflat area. Between 2018 and 2021, the sinkholes developed on the alluvial and colluvial deposits showed higher median rates of areal expansion and volumetric enlargement. However, the median deepening rates were comparable. Single sinkholes in the mudflat experienced a slightly slower percentage areal expansion rate (Table 5).

Concerning the main subsidence mechanism involved in the generation of the sinkholes, the mixed ones show the largest median values for the major axis, perimeter, area, depth, and volume. As expected, collapse sinkholes feature the lowest length-to-depth ratios, whereas sagging sinkholes display the highest ones, with median values of 4.1 and 6.7, respectively. Albeit by a small difference, between 2018 and 2021, the mixed sinkholes recorded the highest median rates of areal expansion, deepening, and volumetric enlargement. All of them experienced an equivalent percentage areal expansion rate whereas, as a consequence of their geometric features, the sagging sinkholes displayed the slowest percentage volumetric enlargement rate (Table 5).

The frequency-size distribution of the mapped sinkholes can be compared with those published from other karst settings to shed light into the influence of geological and hydrogeological factors and various processes (e.g., expansion, coalescence) on the dimensions of the sinkholes. Fig. 12 shows the comparison of the cumulative frequency distribution of the major axis of sinkholes measured in a range of conditions, including carbonate and evaporite karst settings, epigenic and hypogenic systems, as well as bare and mantled areas: (1) in yellow, cover collapse sinkholes in a limestone karst mantled thin unconsolidated alluvium (Val d'Orleans, France; Gombert et al., 2015); (2) in blue, cover subsidence sinkholes in a limestone karst with a thick cohesive cover (Hamedan Plains, Iran; Taheri et al., 2015); (3) in pink, collapse sinkholes in a salt karst with a residual gypsum-rich caprock (Ambal salt pillow, Iran; Gutiérrez and Lizaga, 2016); (4) in green, a wide variety of

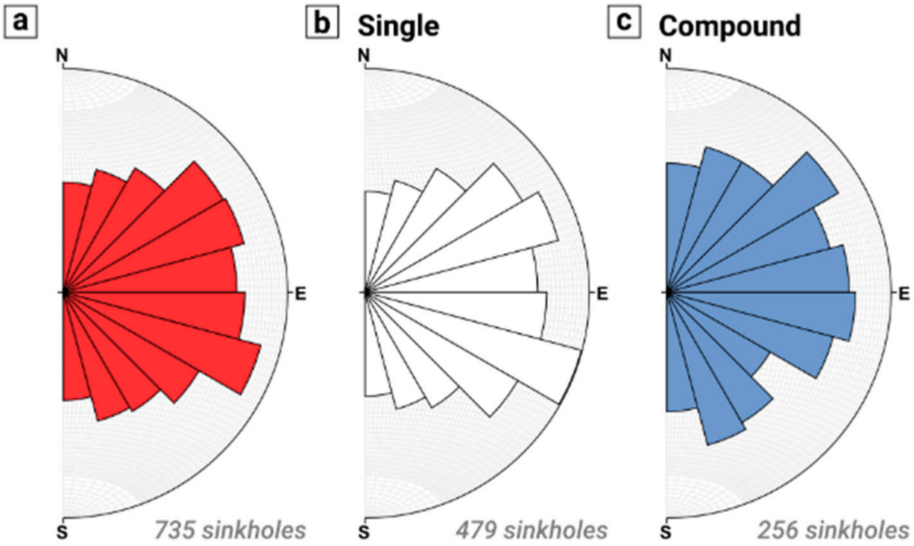

Fig. 11. Half-rose diagrams showing the distribution of the azimuth of the major axes of the elongated sinkholes from 2005 to 2021 (the area of the wedges is proportional to the frequency). (a) All sinkholes, (b) single sinkholes, and (c) compound sinkholes mapped in the study area. Sinkholes were considered elongated if their elongation ratio was smaller than or equal to 0.82. The mean azimuth of all the elongated sinkholes is 89°, while that of the single and compound sinkholes is 90° and 86°, respectively.

sinkholes in an epigene evaporite karst with both unconsolidated covers and lithified caprocks (Fluvia Valley, NE Spain; Gutiérrez et al., 2016); (5) in brown, a hypogene and deep-seated interstratal evaporite karst with a high proportion of caprock collapse sinkholes (Sant Miquel valley, NE Spain; Gutiérrez et al., 2019); (6) in grey, cover subsidence sinkholes developed in the valley floors of the Sivas gypsum karst (B, Sivas, Turkey; Gökkaya et al., 2021); (7) in purple, bedrock collapse sinkholes in the Sivas gypsum karst (A, Sivas, Turkey; Gökkaya et al., 2021); and (8) in red, the sinkholes we have mapped in 2021 in the mantled eogenetic salt karst of the Dead Sea. Like in the other data sets, without distinguishing between single and compound sinkholes. The central part of the distribution of the major axes of the Dead Sea sinkholes is coincident to those inventoried in the Val d'Orleans, characterized by relatively small cover collapse sinkholes developed in thin unconsolidated alluvium underlain by cavernous limestone. However, the Dead Sea sinkholes are larger for cumulative frequencies higher than 0.67 and lower than 0.27. These differences may be attributed to multiple non-exclusive factors, including: (1) the higher cohesion and thickness of the deposits above the soluble material in the Dead Sea; (2) the higher degree of morphological maturity of many sinkholes in the Dead Sea, affected by significant areal enlargement by expansion and coalescence. Note that the major axis of the sinkholes in the Val d'Orleans mostly corresponds to the size of the depressions measured soon after their formation (Gombert et al., 2015). The distribution of the smallest Dead Sea sinkholes within the >0.85 cumulative frequency range is similar to that of the single sinkholes in the Hamedan plains, where there is a thick cohesive cover (Taheri et al., 2015) with higher mechanical strength. The largest major axis measured in the study area (437 m) is in between the largest sinkholes mapped in the salt karst of Gotvand (355 m, Gutiérrez and Lizaga, 2016) and in the evaporite karst of the Fluvia valley (637 m). All of them were compound sinkholes. The database gathered by Gökkaya et al. (2021) in the Sivas gypsum karst differentiates between single and compound sinkholes (solid and dashed lines, respectively, in Fig. 12b), allowing to compare the frequency-size distributions of the major axes in both karst settings. The comparison shows that the sinkholes of the Sivas gypsum karst are larger than those of the Dead Sea salt karst, both for single and compound sinkholes.

As noted above, around 80 % of the sinkholes mapped in 2021 are located inside ten large subsidence basins defined by concentric fissures and scarplets. The dotted lines of Fig. 9 connect the outermost perimetral fissures of those basins. In 2021 these depressions show median values of 142 m, 373 m, and 8535 m^2 for the major axis, perimeter, and area, as well as 9 m and 7152 m^3 for the depth and volume, respectively. The length of the major axes ranges from 32 to 1174 m and their orientation shows preferential NNE-SSW and SE-NW trends. From 2018 to 2021, the median major axis of the subsidence basins did not vary (from 141.7 to 141.6). However, the median perimeter, area, depth, and volume increased by 2, 1, 18, and 15 %, respectively. Eight out of ten basins experienced noticeable areal expansion: six grew to the east (i.e., lakeward) and two to the south (Fig. 9). Despite the areal expansion of the subsidence basins between 2018 and 2021, the total number of sinkholes nested within them slightly decreased from 457 to 454 as result of coalescence processes.

4.3. Spatio-temporal distribution patterns

The 551 sinkholes of 2021 are distributed along a well-defined N-S trending belt, comprising several alignments and linear clusters of tightly packed sinkholes with variable orientations. This spatial distribution strongly suggest that salt dissolution and subsidence are controlled by a concealed fault system with local changes in orientation, as substantiated by Abelson et al. (2003) with geophysical data. Fig. 4 shows the evolution of the spatial distribution of sinkholes between 2005 and 2021. In 2005 there were 158 sinkholes, 106 of which were concentrated in a N-S-oriented linear cluster in the northern sector, south of Mineral Beach resort, and the rest were in several widely spaced clusters, roughly defining a N-S oriented sinkhole-prone belt. The comparison of the multi-temporal sinkhole maps reveals the following spatio-temporal patterns regarding the occurrence of new sinkholes: (1) tend to fill the gaps between the pre-existing clusters along the N-S belt; (2) cause the northward and southward longitudinal extension of the sinkhole belt; (3) transform clusters of closely-spaced sinkholes into large compound depressions; and (4) cause the widening of the sinkhole belt, mainly in the lakeward direction. Overall, sinkholes show a very constrained spatial distribution that expands through time mainly longitudinally and to the east.

The 702 new sinkholes formed between 2005 and 2021 increased the area affected by subsidence from 21,794 to 112,482 m^2 (5362 m^2/year on average), while the overall sinkhole density by number experienced a slight decrease between 2018 and 2021 (Fig. 6). This latter trend is related to sinkhole coalescence, that eventually starts to have a greater impact on the number of sinkholes than the occurrence of new ones, favored by their strongly clustered distribution (i.e., reduction by coalescence exceeds increase by neoformation). Fig. 13 illustrates the spatio-temporal evolution of sinkhole density expressed as number of sinkholes (centroids) by square hectometer with kernel models. The highest density (23 sinkholes/hm^2) occurred in the southern zone in 2011, and subsequently decreased due to sinkhole coalescence.

Table 5

Morphometry of the 2021 sinkholes grouped into single and compound, considering the geomorphic unit in which they occur, and the main subsidence mechanisms inferred from their surface expression. (*): the calculation of the areal and volumetric changes grouping sinkholes by the morpho-sedimentary environment and the main subsidence mechanism has been restricted to single sinkholes. The 'unknown' deepening, areal and volumetric change values indicate the number of sinkholes for which these parameters could not be measured or provided an erroneous value because of (1) insufficient resolution of the data, (2) georeferencing errors, or (3) the evolution of the sinkholes themselves related to processes such as their occurrence and coalescence (see Methodology for further clarification).

	Evolutionary type		Morphosedimentary environment		Main subsidence mechanisms		
	Single (473)	Compound (78)	Alluvial fan and colluvial deposits (82)	Mudflat (469)	Collapse (404)	Mixed (57)	Sagging (90)
Major axis length (m)							
Median (IQR)	5.5 (3.6–8.5)	18.7 (12.5–32.4)	10.4 (7.0–15.5)	5.7 (3.7–10.1)	5.7 (3.6–10.2)	11.5 (6.4–23.1)	6.1 (4.4–12.0)
Mean (range)	7.2 (0.9–60.6)	32.7 (5.9–437.1)	14.5 (1.5–78.4)	10.2 (0.9–437.1)	8.4 (0.9–78.4)	29.9 (2.6–437.1)	9.7 (1.9–43.1)
Perimeter (m)							
Median (IQR)	15.6 (10.2–24.9)	56.3 (35.6–94.2)	29.2 (19.4–44.5)	16.1 (10.3–28.9)	16.2 (10.2–29.1)	33.1 (19.1–69.7)	17.4 (12.2–35.4)
Mean (range)	20.8 (2.5–176.3)	111.3 (16.0–1649.2)	43.0 (4.5–241.3)	32.0 (2.5–1649.2)	24.5 (2.5–241.3)	107.6 (7.7–1649.2)	27.8 (5.1–134.6)
Area (m^2)							
Median (IQR)	17.6 (7.5–44.1)	149.3 (74.0–360.1)	57.1 (25.0–117.9)	19.0 (8.0–59.7)	19.6 (7.6–58.5)	72.7 (26.3–202.8)	22.7 (11.2–70.3)
Mean (range)	51.5 (0.5–2229.4)	1175.5 (17.0–50,410.0)	168.1 (1.5–2229.4)	219.1 (0.5–50,410.0)	67.5 (0.5–2229.4)	1434.0 (4.4–50,410.0)	78.5 (2.0–827.7)
Areal change* (m^2/year)							
Median (IQR) [Δ%/year]	0.9 (0.4–2.2) [5.7]	3.3 (1.4–6.4) [2.2]	3.2 (1.6–6.5) [8.8]	0.7 (0.3–1.5) [5.0]	0.8 (0.4–2.2) [5.7]	1.3 (0.6–3.2) [6.2]	1.1 (0.5–1.5) [6.3]
Mean (range)	2.5 (0.0–100.0)	8.3 (0.5–86.0)	6.6 (0.3–100.0)	1.7 (0.0–42.8)	2.6 (0.0–100.0)	3.2 (0.0–27.1)	1.9 (0.0–14.0)
Unknown	102	43	13	89	93	3	6
Circularity ratio							
Median (IQR)	0.9 (0.9–1.0)	0.6 (0.5–0.8)	0.8 (0.7–0.9)	0.9 (0.9–1.0)	0.9 (0.8–1.0)	0.8 (0.6–0.9)	0.9 (0.8–0.9)
Mean (range)	0.9 (0.4–1.0)	0.6 (0.2–0.9)	0.8 (0.2–1.0)	0.9 (0.2–1.0)	0.9 (0.2–1.0)	0.7 (0.2–1.0)	0.9 (0.4–1.0)
Elongation ratio							
Median (IQR)	0.9 (0.8–0.9)	0.7 (0.7–0.8)	0.8 (0.7–0.9)	0.9 (0.8–0.9)	0.9 (0.8–0.9)	0.8 (0.7–0.9)	0.9 (0.8–0.9)
Mean (range)	0.9 (0.6–1.0)	0.7 (0.5–0.9)	0.8 (0.5–0.9)	0.9 (0.5–1.0)	0.9 (0.5–1.0)	0.8 (0.5–0.9)	0.8 (0.6–1.0)
Depth (m)							
Median (IQR)	1.2 (0.7–2.6)	3.3 (2.3–5.6)	3.4 (2.2–5.6)	1.3 (0.7–2.6)	1.6 (0.7–3.1)	2.2 (1.3–4.8)	1.1 (0.6–1.8)
Mean (range)	2.0 (0.1–12.6)	4.4 (1.3–21.2)	4.1 (0.2–12.6)	2.0 (0.1–21.2)	2.3 (0.1–12.6)	3.5 (0.2–21.2)	1.4 (0.1–4.4)
Length to depth ratio							
Median (IQR)	4.3 (3.2–5.8)	5.7 (4.1–8.4)	3.4 (2.7–4.1)	4.6 (3.6–6.4)	4.1 (3.0–5.3)	5.7 (3.9–8.8)	6.7 (4.9–8.4)
Mean (range)	4.9 (1.1–28.9)	6.6 (3.0–20.7)	3.9 (1.1–13.0)	5.4 (1.2–28.9)	4.5 (1.1–16.6)	6.8 (2.0–20.7)	7.2 (3.1–28.9)
Deepening rate (cm/year)							
Median (IQR)	5.8 (3.3–9.8)	7.5 (3.6–26.39)	6.1 (4.1–12.7)	5.8 (3.2–10.1)	6.1 (3.2–10.2)	7.9 (4.1–15.0)	5.2 (3.2–7.3)
Mean (range)	9.1 (0.1–131.0)	22.9 (0.4–202.5)	12.1 (0.1–94.4)	10.5 (0.2–202.5)	10.2 (0.1–131.0)	21.9 (0.4–202.5)	6.2 (0.2–28.4)
Unknown	157	36	35	158	164	15	14
Volume (m^3)							
Median (IQR)	4.4 (0.8–24.4)	68.4 (40.0–409.5)	39.5 (8.7–160.9)	4.8 (0.8–32.6)	6.2 (0.8–38.9)	22.5 (5.2–197.5)	4.2 (1.2–17.5)
Mean (range)	76.9 (0.0–4093.0)	3790.2 (2.9–228,342.6)	302.4 (0.0–4366.0)	658.7 (0.0–228,342.6)	120.3 (0.0–4366.0)	4925.8 (0.1–228,342.6)	30.5 (0.0–353.1)
Volumetric change* (m^3/year)							
Median (IQR) [Δ%/year]	0.3 (0.1–1.3) [9.1]	5.7 (2.5–61.9) [7.8]	1.9 (0.9–5.4) [8.5]	0.3 (0.1–0.8) [12.0]	0.4 (0.1–1.4) [11.1]	0.6 (0.3–1.8) [11.3]	0.2 (0.1–0.8) [7.4]
Mean (range)	4.5 (0.0–468.3)	967.1 (0.3–41,686.4)	18.2 (0.0–468.3)	1.8 (0.0–57.6)	5.7 (0.0–468.3)	1.2 (0.0–5.5)	1.6 (0.0–57.5)
Unknown	151	26	20	131	137	5	9

Similarly, the northern sector reached its maximum density (13 sinkholes/hm^2) in 2008 and then it decreased by the merging of progressively larger compound sinkholes. In contrast, in the central sector of the belt, where the sinkhole landscape shows a lower degree of maturity, sinkhole density shows a general increase over the whole investigation period.

The Nearest Neighbor Index (NNI) has been widely used to assess the spatial clustering versus dispersion of sinkholes (De Waele and Gutiérrez, 2022 and references therein). This is an important parameter from the spatial prediction perspective, in as much as the location of future sinkholes is easier to predict in areas where sinkholes tend to have a clustered distribution (Gutiérrez, 2016). A NNI of 0 means maximum aggregation, a NNI of 1 random distribution, and 2.1491 maximum dispersion. From 2005 to 2021 the sinkholes showed a highly clustered distribution with a mean NNI of 0.45 (range: 0.42–0.47). This value is comparable to other karstic areas with clustered sinkhole patterns such as the caprock- collapse sinkholes of the Ambal salt pillow, Zagros Mountains – Iran (NNI: 0.3; Gutiérrez and Lizaga, 2016) or the cover-collapse sinkholes triggered by flooding of the Flint River in a covered limestone karst in Albany, Georgia – USA (NNI: 0.55; Hyatt and Jacobs, 1996). Moreover, in 2021 sinkholes in the mudflat show higher clustering than in the alluvial and colluvial deposits (0.44 and 0.80, respectively), and sagging and collapse sinkholes show a slightly higher clustering than mixed ones (0.39, 0.47, and 0.60, respectively).

The clustering of the sinkholes can be also assessed using the spatially distributed DBSCAN algorithm (Ester et al., 1996). Considering a threshold of 3 sinkholes as the minimum number of centroids in a cluster and a maximum grouping distance of 55 m between points,

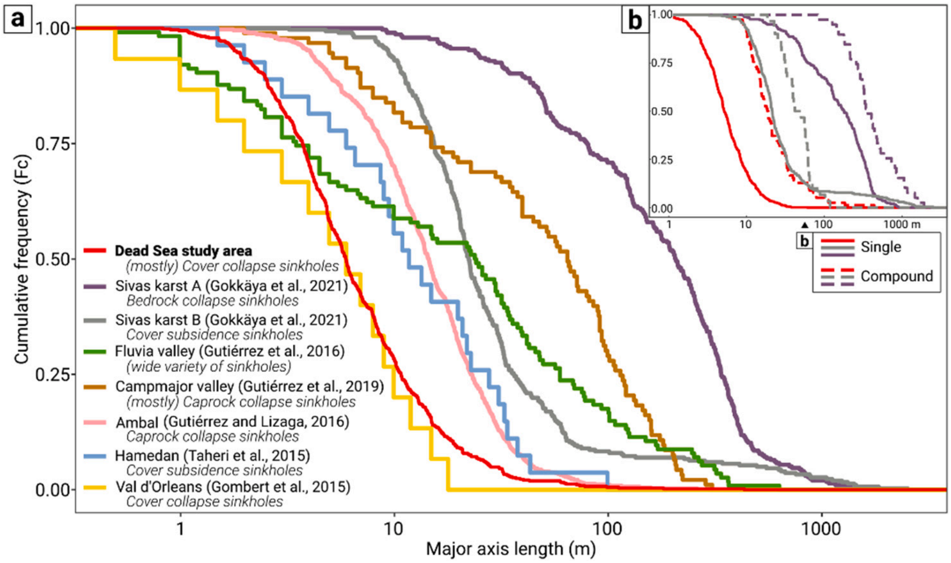

Fig. 12. Cumulative frequency distribution plot of the major axis of the sinkholes mapped in different karst regions worldwide (a), and differentiating single sinkholes (solid lines) from compound sinkholes (dashed line) inventoried in the Sivas gypsum karst and in this work (b). Both plots share the same legend. See text for description. The number of steps informs about the quantity of data, as each one corresponds to an observation (i.e., smoother lines indicate more extensive databases).

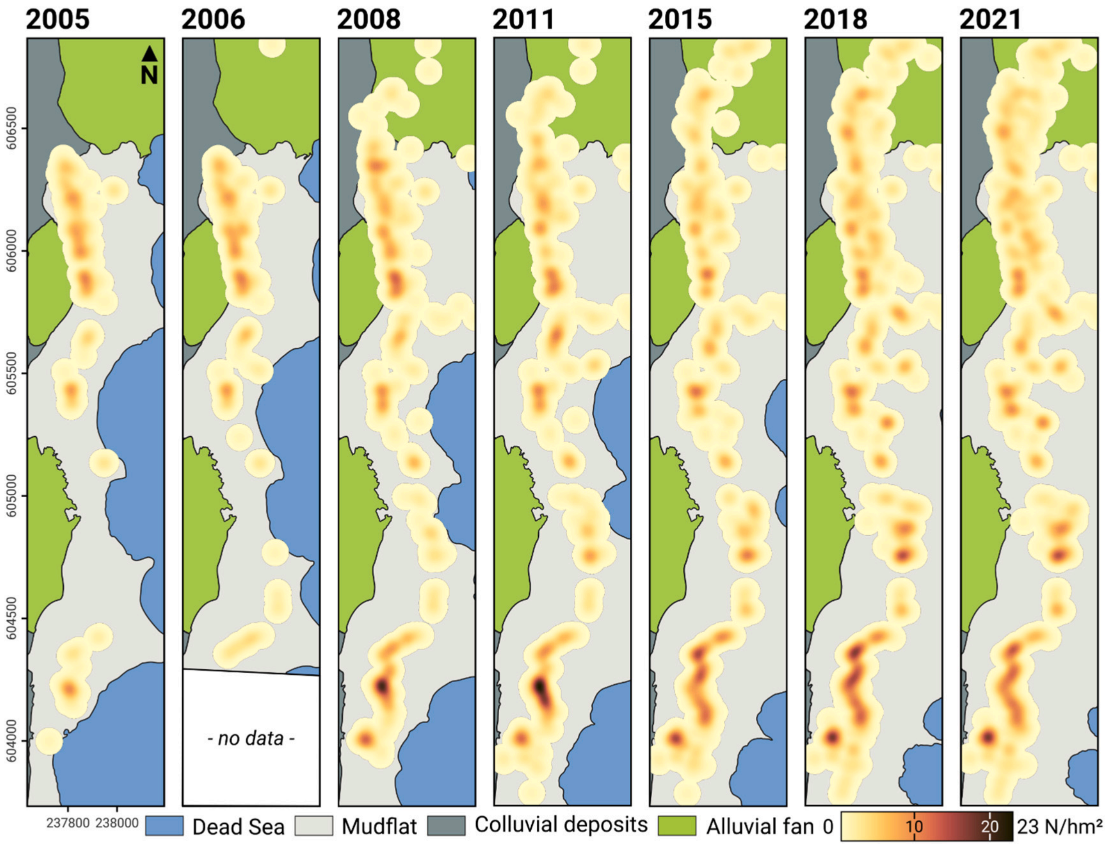

Fig. 13. Kernel density models produced with the centroids of the sinkholes showing the spatio-temporal evolution of sinkhole density (number of sinkholes/hm^2). Note that in some sectors (e.g., southern zone) sinkhole density increases and eventually starts to decrease due to coalescence.

calculated with a nearest neighbor graph for the 2021 sinkholes, it identified 17 outliers and 9 clusters containing 534 sinkholes (Fig. 9f). There is a tight spatial correlation between the location of the sinkhole clusters identified by the DBSCAN algorithm and the large subsidence basins defined by concentric fissures. As many as 97 % and 80 % of the sinkholes mapped in 2021 belong to a cluster or are located inside one of the subsidence basins, respectively. In addition, only 3 clusters including a total of 12 sinkholes are not located within any of the mapped subsidence basins (Fig. 9f).

5. Discussion

5.1. Sinkhole characteristics and spatio-temporal evolution

The eogenetic salt karst of the Dead Sea is one of the most striking examples of human-induced sinkhole hazard worldwide. Its rapid development in an expanding lake shore is causing significant societal and economic damage that require a good understanding of the subsidence phenomena for the design and application of effective mitigation measures. Moreover, this highly dynamic hazardous process also offers an exceptional opportunity to study the morphometric and spatio-temporal evolution of sinkholes using high-resolution data covering a limited time span. Time-lapse cartographic inventories allowed the reconstruction of the sinkhole evolutionary patterns between 2005 and 2021 (16.9 years), and the high-quality SfM-derived data from 2018 and 2021 provided the basis for an innovative three-dimensional characterization. This work illustrates that multi-temporal sinkhole analyses yield valuable clues about the geological processes and factors involved in these hazardous phenomena and provide an objective basis for the development of reliable spatial predictions.

The sinkholes in the study area are concentrated within a narrow N-S-oriented strip including alignments and tight clusters with NE to SSE trends (Fig. 4). This spatial distribution, which coincides with the principal trends of the basin-bounding faults, strongly suggests that salt dissolution and sinkhole development are controlled by concealed intrabasinal faults, as corroborated by geophysical data (e.g., Abelson et al., 2003). Fault systems can control the location of sinkholes by (Fig. 2): (1) guiding the upward flow of undersaturated water from deep bedrock aquifers; (2) creating permeability pathways and barriers within the halite-bearing cover; and (3) reducing the mechanical strength of the cover. The deep source of the groundwater likely responsible for a hypogene salt dissolution is supported by the existence of thermal water springs along the coast, such as Mineral Beach (19–43 °C) and Ein Kedem (28–48 °C) (Shalev and Yechieli, 2007; Zilberman et al., 2017), and subaqueous groundwater discharge (e.g., Ionescu et al., 2012). In addition, syn- and post-sedimentary fault activity may have controlled the depth, thickness, and lateral extension of the salt unit, as suggested by Ezersky and Frumkin (2013).

The vast majority of the sinkholes mapped are single, small, relatively shallow, subcircular, collapse depressions. They show significant differences depending on the geomorphic unit in which they develop. In general, sinkholes in the slightly cemented gravelly alluvial and colluvial deposits are larger than those developed in the soft deposits of the mudflat (Table 5). Their cohesive behaviour and the development of collapse failures may prevent from the generation of suffosion sinkholes. The length-to-depth ratio tends to be larger in the sinkholes of the mudflat than those mapped in alluvial and colluvial deposits, with average values of 5.4 and 3.9, respectively. This can be largely attributed to the rapid expansion of the former by slumping. The obtained values are rather similar to those reported in Ghor Al-Haditha area on the eastern shore of the Dead Sea (7.14 in mudflat and 2.5 in alluvial fans, measured as depth-to-diameter by Al-Halbouni et al., 2017). Interestingly, about 80 % of the 2021 sinkholes are located within 10 large subsidence basins up to 1174 m long defined by concentric fissures and scarplets associated with gentle inward-facing flexures. These basins have been mapped for the first time on the western coast thanks to the high-resolution SfM-derived orthomosaics from 2018 and 2021, which allowed us to identify the outermost fissures that display the smallest opening, throw and lateral continuity (Fig. 9).

On average, the area of the single sinkholes mapped in the alluvial-colluvial deposits and in the mudflat grew 13 and 9 % over ten years (2008–2018), respectively, largely due to mass wasting processes acting on their steep margins. This means that the depressions result from both dissolution-induced subsidence and slope movements, with a progressively higher contribution of the latter as the sinkholes become more mature. Collapse sinkholes in gravelly deposits mostly expand by falls and topples controlled by concentric unloading cracks, whereas rotational sliding is the main process acting in the mudflat sinkholes (Fig. 7b and e). From 2018 to 2021 these mass wasting processes were the main responsible for a median areal increase rate of 0.9 m^2/year in single sinkholes. Slope movements at the margins of the sinkholes involve an increase in their area, but not in their volume, since the landslide deposits contribute to fill the depressions and experience a volume expansion (bulking effect). This explains the limited volumetric enlargement computed for the single sinkholes between 2018 and 2021 (median growth rate of 0.3 m^3/year), largely attributable to renewed subsidence. From 2005 to 2021 the areal expansion rates remained essentially constant, with median values ranging between 0.7 (2015) and 1.1 m^2/year (2008), against the concept whereby steadily expanding sinkholes experience progressively faster areal increase as their perimeter grows (De Waele and Gutiérrez, 2022). We hypothesize that the retrogressive progression of rotational slides in the margins of the mudflat sinkholes produces the flattening of the slopes with a stabilizing effect, i.e., expansion is not steady, but experiences a declining trend. Single collapse sinkholes in the mudflat are the most common in the study area and experience a slower areal expansion rate than those in the alluvial fan and colluvial deposits (Table 5).

The tightly clustered distribution of the sinkholes in the study area determines that coalescence plays a critical role in their evolution. Sinkhole coalescence may occur via two mechanisms: (1) lateral expansion of adjoining sinkholes; (2) occurrence of new sinkholes intersecting pre-existing ones (Fig. 8c–c′). This process has a number of effects on the morphometric features of the sinkholes, including an increase in their area, elongation, and length-to-depth ratio. It also causes a decrease in their number, density by number and circularity (Table 5; Figs. 6, 13). This work illustrates that those metrics in sinkhole fields are conditioned by the initial distribution pattern of the sinkholes (clustered versus dispersed) and the maturity of the karst landscape, as illustrated with theoretical exercises by De Waele and Gutiérrez (2022).

The comparison of the multi-temporal sinkhole maps provides the basis for understanding the spatio-temporal patterns of new sinkhole occurrence and the growth of the pre-existing ones, including the large subsidence depressions. From 2005 to 2021 sinkholes have been essentially confined within a N-S trending belt, and clusters and alignments mostly expanded longitudinally, filling gaps, and to the east (Fig. 4). This eastward migration of sinkhole occurrence explains the prevalent rough E-W orientation of the major axes of the elongated sinkholes (Fig. 11). The large subsidence basins have experienced a similar evolution. Six out of ten expanded lakeward and two to the south. It can be forecast that eventually most of them will connect longitudinally, forming large elongated compound sinkholes like the one mapped in the northern sector of the area, where the landscape shows a greater degree of maturity (Figs. 4 and 9). The consistent spatio-temporal evolution of the subsidence basins and sinkhole alignments and clusters can be attributed to preferential dissolution controlled by concealed faults and the lakeward migration of a dissolution front, both processes occurring at significant distance to the west of the current position of the brackish-saline water interface. Fault-guided upward flow of undersaturated groundwater from bedrock aquifers is most probably contributing to the dissolution processes (hypogene karst), as supported by the presence of thermal water springs. The eastward migration of a dissolution front is most probably dictated by the gradient of the hydrologic system, which base level corresponds to the declining Dead Sea lake.

The total volumetric increase of the sinkholes between 2018 and 2021 (151,792 m^3) provides a minimum estimate of the yearly volume of salt dissolved beneath the area affected by sinkholes, equivalent to a cube with an edge of 37 m. The actual value can be considerably higher because not all the void space created by dissolution produces subsidence and the collapsed sediments are affected by a bulking effect. Considering the area affected by sinkholes in 2021 (112,482 m^2), an average subsidence rate of 45 cm/year can be estimated. Al-Halbouni et al. (2017) calculated an average subsidence rate of 21 cm/year on the eastern coast of the Dead Sea. In their study they considered both the Ghor Al-Haditha subsidence depression and the nested sinkholes. These are very high values compared with other salt karst environments. For example, the fastest sinkhole monitored in the alluvial evaporite karst of the semiarid Ebro Valley (Spain) related to halite dissolution shows mean and maximum subsidence rates of 5.44 and 16.28 cm/year, respectively (Desir et al., 2018). In Russell County, Kansas, two sagging sinkholes hundreds of meters across related to the interstratal dissolution of Permian salts at a depth of 350 m experienced maximum subsidence rates of 10–13 cm/year. These sinkholes were induced by improperly plugged oil wells that allowed fresh water to flow downwards through the salt (Croxton, 2003). In north Cheshire, UK, Serridge and Cooper (2022) report subsidence rates of 15–35 cm/year in a subsidence basin related to dissolution of Triassic salt induced by uncontrolled brine extraction. The high dissolution and subsidence rates in the Dead Sea arid environment (70 mm of mean annual rainfall) support that rising groundwater flows from a deep aquifer with a distant recharge area play a significant role in the karstification process (Abelson et al., 2003, 2017; Closson, 2005; Shalev et al., 2006; Charrach, 2019). According to Abelson et al. (2017), sinkhole development on the western shore of the Dead Sea is controlled with some delay response by the flux of fresh groundwater fed by rainfall in the more humid Judea Mountains (300–600 mm of average annual precipitation), located >30 km to the west.

The available borehole and geophysical data indicate that the study area is underlain by a thick salt layer at shallow depth, which is vertically offset by concealed faults (Abelson et al., 2003, 2006; Yechieli et al., 2006). Consistently with previous studies carried out in the western shore of the Dead Sea, we attribute the formation of sinkholes to salt dissolution (i.e., dissolution model). This subsurface karstification process is most probably controlled by faults that guide groundwater flow, but may also occur along the salt edge and can migrate lakeward though the propagation of a dissolution front. We consider that the dissolution-piping model proposed on the eastern shore, largely attributing sinkhole development to conduit networks created by subsurface erosion in muds, is not compatible with the analysed sinkholes due to the following reasons: (1) piping conduits cannot generate collapse sinkholes with diameters as much as 32 m at the time of formation in the mudflat; (2) piping cannot explain the numerous sinkholes mapped in the alluvial fans, underlain by pebble-cobble gravel, too coarse for internal erosion; (3) the subsurface mass depletion computed in the study area for the interval 2018–2021, with a minimum volume of 151,792 m^3 and an minimum average thickness of 1.34 m for the material removed from the subsurface, cannot be explained by the erosion and evacuation of detrital material from a conduit network, but by rapid dissolution of high solubility halite; (4) the spatial distribution of sinkholes, forming rather rectilinear NNW-SSE to NE-SW alignments, is not consistent with a putative network of piping conduits, which should have a dominant east-directed trend controlled by the hydraulic gradient.

5.2. Sinkhole susceptibility models

A major challenge in the Dead Sea with direct implications for risk management is the prediction of the spatial distribution of future sinkholes. This involves the production of sinkhole susceptibility models with a reasonably high prediction capability. Preferably, such models should be able to forecast a large percentage of the new sinkholes delineating high susceptibility zones that represent a small proportion of the total area. Susceptibility models are commonly developed analysing the statistical relationships between the spatial distribution of sinkholes and that of a number of controlling factors (Gutiérrez, 2016 and references therein). This approach is hardly feasible in the Dead Sea, given the lack of information on the hidden factors that control the dissolution and subsidence processes. Nonetheless, detailed cartographic sinkhole inventories and the analysis of the spatial-temporal evolution patterns of the sinkholes offer the possibility of developing susceptibility models solely based on past sinkhole occurrence. These models are typically based on the assumption that future sinkholes will show spatial distribution patterns similar to those in the past, and that the existing sinkholes are good predictors for future ones (Gutiérrez, 2016). The performance of susceptibility models based on sinkhole inventories is particularly satisfactory in karst areas where sinkholes show a clustered distribution, as is the case of the Dead Sea. Moreover, susceptibility models solely based on sinkhole inventories and spatially distributed parameters derived from them (e.g., density, proximity) often yield prediction rates as high as those developed through more complex and time-consuming statistical approaches incorporating multiple factors (e.g., Galve et al., 2009). In our study area, over a period of 16 years (2005–2021), sinkholes have been restricted to a N-S trending belt that has experienced a progressive expansion toward the lake (Fig. 4). This spatio-temporal pattern can be used as the basis to produce simple susceptibility models. For instance, the delineation of a high susceptibility zone using buffers 50 m and 100 m wide to the west and east, respectively, of an axis connecting the antipodal points of the main sinkhole clusters from 2008, would allow to predict 83 % of the new sinkholes formed in the following decade (2008–2018; Fig. 14a). This is a high prediction rate achieved with a restricted high susceptibility area (19 % of the study area), applying a simple method and considering a reasonable time lapse from the risk management perspective (i.e., high benefit/effort ratio). Moreover, the large subsidence basins mapped thanks to the SfM-derived data, which host a great proportion of the sinkholes, can be used for spatial predictions. For instance, 71 % of the new sinkholes occurred between 2018 and 2021 fall within the large subsidence basins mapped in 2018, which represent 10 % of the study area (Fig. 14b).

6. Conclusions

The methodology presented in this work, essentially based on multitemporal cartographic sinkhole inventories with morphometric data, allowed us to quantitatively analyse the morphological evolution of the sinkholes and their spatio-temporal patterns. This information provides an objective basis for gaining insight into the origin of the sinkholes and furnishing hazard assessments.

The sinkholes are concentrated within a well-defined N-S-oriented strip, including alignments and tight clusters that have expanded to the east (lakeward) and longitudinally, filling gaps between them. Most of the sinkholes are single, small, relatively shallow, subcircular, and of the collapse type. The vast majority of the sinkholes (80 % in 2021) occur within large subsidence basins defined by gentle flexures, fissures and scarplets.

Over ten years (2008–2018), single sinkholes in alluvial and colluvial deposits and in the mudflat experienced areal growths of 13 and 9 %, respectively, revealing the important morphogenetic role played by mass wasting processes in the post-collapse development of the depressions. The rapid lateral expansion of collapse and mixed sinkholes by mass wasting processes, the high rate of sinkhole occurrence, and the tightly clustered distribution determines that sinkhole coalescence plays an important role in the time-dependent morphometric and spatial features of the sinkholes.

Between 2018 and 2021 the area affected by sinkholes experienced an average subsidence rate of 45 cm/year. This high value illustrates the extremely rapid dissolution of the salt unit despite the arid conditions. Sinkhole clusters are expected to evolve into large compound sinkholes that will progressively merge to form a large lakeward propagating subsidence trough.

Several lines of evidence support the hypogenic origin of the Dead Sea salt karst by rising groundwater flows from deep aquifers guided by concealed faults: (1) the rectilinear sinkhole distribution, coincident with the main trends of the basin-bounding faults, (2) the consistent spatial distribution over time of the sagging basins and the sinkhole alignments and clusters, (3) the presence of thermal water springs, and (4) the high dissolution and subsidence rates calculated in such an arid environment.

Finally, this work illustrates that detailed multi-temporal sinkhole mapping provides the basis for predicting the spatial distribution of future sinkholes with a high success rate and a high benefit/effort ratio.

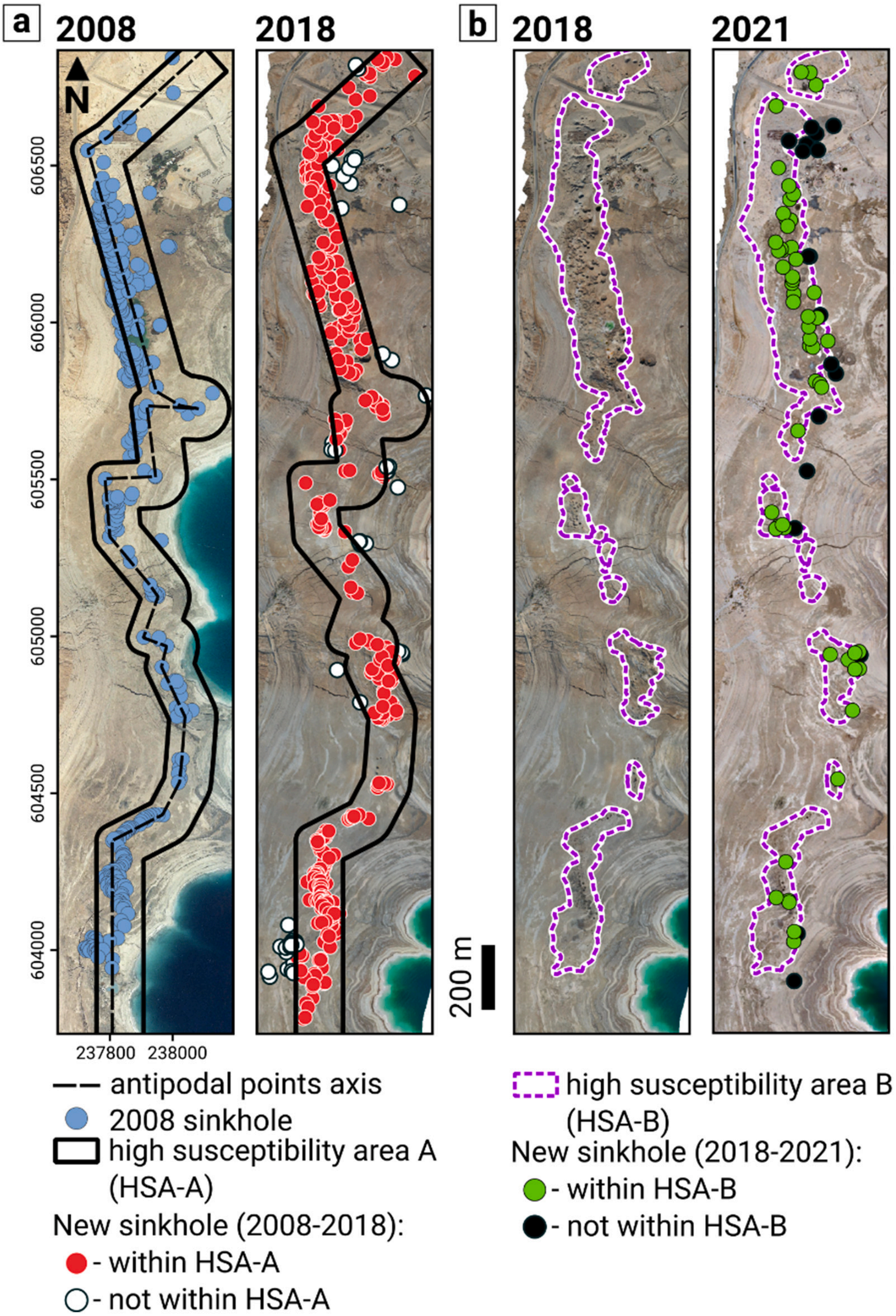

Fig. 14. Susceptibility models based in the spatio-temporal patterns observed in the study area. a. A high susceptibility area, based in an asymmetric buffer away from an axis connecting the antipodal points of the main 2008 sinkhole clusters (19 % of the study area), allows to predict 83 % of the new sinkholes formed in the following decade 2008–2018. b. A high susceptibility area restricted to the large subsidence basins (10 % of the study area) mapped in 2018 serves to predict 71 % of the new sinkholes occurred from 2018 to 2021. Sinkholes represented as centroids.

Declaration of competing interest

The authors declare that they have no known competing financial interests or personal relationships that could have appeared to influence the work reported in this paper.

Data availability

Data will be made available on request.

Acknowledgments

This work has been supported by projects CGL2017-85045-P and PID2021_123189NB-I00 (Ministerio de Ciencia, Innovación y Universidades, Gobierno de España). J. Sevil has a predoctoral contract (PRE2018-084240) cofinanced by the Spanish Government (Ministerio de Ciencia, Innovación y Universidades, Gobierno de España) and the European Social Fund (ESF). The authors would like to thank the Geological Survey of Israel, and in particular Yoseph Yechieli, Gidon

Baer and Meir Abelson for their valuable help and for providing aerial photographs and satellite data.

References

Abelson, M., Baer, G., Shtivelman, V., Wachs, D., Raz, E., Crouvi, O., Kurzon, I., Yechieli, Y., 2003. Collapse-sinkholes and radar interferometry reveal neotectonics concealed within the Dead Sea basin. Geophys. Res. Lett. 30 (10) https://doi.org/10.1029/2003gl017103.

Abelson, M., Yechieli, Y., Crouvi, O., Baer, G., Wachs, D., Bein, A., Shtivelman, V., 2006. Evolution of the Dead Sea Sinkholes. https://doi.org/10.1130/2006.2401(16).

Abelson, M., Yechieli, Y., Baer, G., Lapid, G., Behar, N., Calvo, R., Rosensaft, M., 2017. Natural versus human control on subsurface salt dissolution and development of thousands of sinkholes along the Dead Sea coast. Journal of Geophysical Research: Earth Surface 122 (6), 1262–1277. https://doi.org/10.1002/2017JF004219.

Abou Karaki, N., Fiaschi, S., Closson, D., 2016. Sustainable development and anthropogenic induced geomorphic hazards in subsiding areas. Earth Surf. Process. Landf. 41 (15), 2282–2295. https://doi.org/10.1002/esp.4047.

Abou Karaki, N., Fiaschi, S., Paenen, K., Al-Awabdeh, M., Closson, D., 2019. Exposure of tourism development to salt karst hazards along the Jordanian Dead Sea shore. Hydrol. Earth Syst. Sci. 23, 2111–2127. https://doi.org/10.5194/hess-23-2111-2019.

Al-Halbouni, D., Holohan, E.P., Saberi, L., Alrshdan, H., Sawarieh, A., Closson, D., Walter, T.R., Dahm, T., 2017. Sinkholes, subsidence and subrosion on the eastern shore of the Dead Sea as revealed by a close-range photogrammetric survey. Geomorphology 285, 305–324. https://doi.org/10.1016/j.geomorph.2017.02.006.

Al-Halbouni, D., Holohan, E.P., Taheri, A., Schöpfer, M.P.J., Emam, S., Dahm, T., 2018. Geomechanical modelling of sinkhole development using distinct elements: model verification for a single void space and application to the Dead Sea area. Solid Earth 9, 1341–1373. https://doi.org/10.5194/se-9-1341-2018.

Al-Halbouni, D., Holohan, E.P., Taheri, A., Watson, R.A., Polom, U., Schöpfer, M.P.J., Emam, S., Dahm, T., 2019. Distinct element geomechanical modelling of the formation of sinkhole clusters within large-scale karstic depressions. Solid Earth 10 (4), 1219–1241. https://doi.org/10.5194/se-10-1219-2019.

Al-Halbouni, D., Watson, R.A., Holohan, E.P., Meyer, R., Polom, U., Dos Santos, F.M., Comas, X., Alrshdan, H., Krawczyk, C.M., Dahm, T., 2021. Dynamics of hydrological and geomorphological processes in evaporite karst at the eastern Dead Sea – a multidisciplinary study. Hydrol. Earth Syst. Sci. 25 (6), 3351–3395. https://doi.org/10.5194/hess-25-3351-2021.

Arav, R., Filin, S., Avni, Y., 2020. Sinkhole swarms from initiation to stabilisation based on in situ high-resolution 3-D observations. Geomorphology 351, 106916. https://doi.org/10.1016/j.geomorph.2019.106916.

Avni, Y., Lensky, N., Dente, E., Shviro, M., Arav, R., Gavrieli, I., Yechieli, Y., Abelson, M., Lutzky, H., Filin, S., Haviv, I., 2016. Self-accelerated development of salt karst during flash floods along the Dead Sea Coast, Israel. J. Geophys. Res. Earth Surf. 121 (1), 17–38. https://doi.org/10.1002/2015jf003738.

Baer, G., Schattner, U., Wachs, D., Sandwell, D., Wdowinski, S., Frydman, S., 2002. The lowest place on Earth is subsiding—An InSAR (interferometric synthetic aperture radar) perspective. GSA Bull. 114 (1), 12–23. https://doi.org/10.1130/0016-7606(2002)114<0012:TLPOEI>2.0.CO;2.

Ben-Avraham, Z., Garfunkel, Z., Lazar, M., 2008. Geology and Evolution of the Southern Dead Sea Fault with Emphasis on Subsurface Structure. Annu. Rev. Earth Planet. Sci. 36 (1), 357–387. https://doi.org/10.1146/annurev.earth.36.031207.124201.

Bernatek-Jakiel, A., Poesen, J., 2018. Subsurface erosion by soil piping: significance and research needs. Earth Sci. Rev. 185, 1107–1128. https://doi.org/10.1016/j.earscirev.2018.08.006.

Charrach, J., 2019. Investigations into the Holocene geology of the Dead Sea basin. Carbonates Evaporites 34 (4), 1415–1442. https://doi.org/10.1007/s13146-018-0454-x.

Chiba, T., Kaneta, S.-I., Suzuki, Y., 2008. Red relief image map: new visualization method for three dimensional data. Int. Arch. Photogramm. Remote. Sens. Spat. Inf. Sci. 37 (B2), 1071–1076. Retrieved from. https://www.isprs.org/proceedings/XXXVII/congress/2_pdf/11_ThS-6/08.pdf.

Clark, P.J., Evans, F.C., 1954. Distance to nearest neighbor as a measure of spatial relationships in populations. Ecology 35 (4), 445–453. https://doi.org/10.2307/1931034.

Closson, D., 2005. Structural control of sinkholes and subsidence hazards along the Jordanian Dead Sea coast. Environ. Geol. 47 (2), 290–301. https://doi.org/10.1007/s00254-004-1155-4.

Closson, D., Abou Karaki, N., 2009a. Human-induced geological hazards along the Dead Sea coast. Environ. Geol. 58 (2), 371–380. https://doi.org/10.1007/s00254-008-1400-3.

Closson, D., Karaki, N.A., 2009b. Salt karst and tectonics: Sinkholes development along tension cracks between parallel strike-slip faults, Dead SeaJordan. Earth Surface Processes and Landforms 34 (10), 1408–1421. https://doi.org/10.1002/esp.1829.

Closson, D., Pasquali, P., Riccardi, P., Milisavljevic, N., Abou Karaki, N., 2013. The water deficit in the Middle East and the disappearance of the Dead Sea. In: Boever, M. De, Khlosi, M., Delbecque, N., Pue, J. De, Ryken, N., Verdoodt, A., et al. (Eds.), Desertification and Land Degradation: Processes and Mitigation. UNESCO Chair of Eremology, Ghent University, Belgium, pp. 16–24.

Coianiz, L., Bialik, O.M., Ben-Avraham, Z., Lazar, M., 2019. Late Quaternary lacustrine deposits of the Dead Sea basin: high resolution sequence stratigraphy from downhole logging data. Quat. Sci. Rev. 210, 175–189. https://doi.org/10.1016/j.quascirev.2019.03.009.

Coianiz, L., Schattner, U., Lang, G., Ben-Avraham, Z., Lazar, M., 2020. Between plate and salt tectonics—new stratigraphic constraints on the architecture and timing of the Dead Sea basin during the late Quaternary. Basin Res. 32 (4), 636–651. https://doi.org/10.1111/bre.12387.

Croxton, N.M., 2003. Subsidence on Interstate 70 in Russell County, Kansas, related to salt dissolution-a history. In: Evaporite Karst and Engineering/Environmental Problems in the United States: Oklahoma Geological Survey Circular, 109, pp. 149–155.

De Waele, J., Gutiérrez, F., 2022. Karst Hydrogeology, Geomorphology and Caves. John Wiley & Sons.

Desir, G., Gutiérrez, F., Merino, J., Carbonel, D., Benito-Calvo, A., Guerrero, J., Fabregat, I., 2018. Rapid subsidence in damaging sinkholes: Measurement by high-precision leveling and the role of salt dissolution. Geomorphology 303, 393–409. https://doi.org/10.1016/j.geomorph.2017.12.004.

Dor, Y.B., Neugebauer, I., Enzel, Y., Schwab, M.J., Tjallingii, R., Erel, Y., Brauer, A., 2019. Varves of the Dead Sea sedimentary record. Quat. Sci. Rev. 215, 173–184. https://doi.org/10.1016/j.quascirev.2019.04.011.

Dowle, M., Srinivasan, A., 2022. data.table: Extension of 'data.frame'. Retrieved from. https://CRAN.R-project.org/package=data.tableEvans.

Ester, M., Kriegel, H.-P., Sander, J., Xu, X., 1996. A density-based algorithm for discovering clusters in large spatial databases with noise. Retrieved from. In: kdd, 96. aaai.org, pp. 226–231. https://www.aaai.org/Papers/KDD/1996/KDD96-037.pdf?source=post_page.

Evans, J.S., Murphy, M.A., 2021. spatialEco. https://github.com/jeffreyevans/spatialEco. Retrieved from.

Ezersky, M., Frumkin, A., 2013. Fault — Dissolution front relations and the Dead Sea sinkhole problem. Geomorphology 201, 35–44. https://doi.org/10.1016/j.geomorph.2013.06.002.

Ezersky, M., Frumkin, A., 2020. Identification of sinkhole origin using surface geophysical methods, Dead SeaIsrael. Geomorphology 364, 107225. https://doi.org/10.1016/j.geomorph.2020.107225.

Ezersky, M., Eppelbaum, L., Legchenko, A., Al-Zoubi, A., Abueladas, A.A., 2021. Salt layer characteristics in the Ghor Al-Haditha area, Jordan: comprehensive combined reprocessing of geophysical data. Environ. Earth Sci. 80, 1–20. https://doi.org/10.1007/s12665-021-09373-4.

Ezersky, M., Legchenko, A., Camerlynck, C., Al-Zoubi, A., 2009. Identification of sinkhole development mechanism based on a combined geophysical study in Nahal Hever South area (Dead Sea coast of Israel). Environ. Geol. 58 (5), 1123–1141. https://doi.org/10.1007/s00254-008-1591-7.

Festa, V., Fiore, A., Parise, M., Siniscalchi, A., 2012. Sinkhole evolution in the Apulian Karst of Southern Italy: a case study, with some considerations on Sinkhole Hazards. J. Cave Karst Stud. 74 (2), 137–147. https://doi.org/10.4311/2011JCKS0211.

Filin, S., Baruch, A., Avni, Y., Marco, S., 2011. Sinkhole characterization in the Dead Sea area using airborne laser scanning. Nat. Hazards 58 (3), 1135–1154. https://doi.org/10.1007/s11069-011-9718-7.

Frumkin, A., Raz, E., 2001. Collapse and subsidence associated with salt karstification along the Dead Sea. Carbonates Evaporites 16 (2), 117–130. https://doi.org/10.1007/BF03175830.

Frumkin, A., Ezersky, M., Al-Zoubi, A., Akkawi, E., Abueladas, A.-R., 2011. The Dead Sea sinkhole hazard: geophysical assessment of salt dissolution and collapse. Geomorphology 134 (1–2), 102–117. https://doi.org/10.1016/j.geomorph.2011.04.023.

Galve, J.P., Gutiérrez, F., Lucha, P., Guerrero, J., Bonachea, J., Remondo, J., Cendrero, A., 2009. Probabilistic sinkhole modelling for hazard assessment. Earth Surf. Process. Landf. 34 (3), 437–452. https://doi.org/10.1002/esp.1753.

Garfunkel, Z., Ben-Avraham, Z., 1996. The structure of the Dead Sea basin. Tectonophysics 266 (1–4), 155–176. https://doi.org/10.1016/s0040-1951(96)00188-6.

Gökkaya, E., Gutiérrez, F., Ferk, M., Görüm, T., 2021. Sinkhole Development in the Sivas Gypsum Karst. Geomorphology, Turkey. https://doi.org/10.1016/j.geomorph.2021.107746.

Gombert, P., Orsat, J., Mathon, D., Alboresha, R., Al Heib, M., Deck, O., 2015. Role des effondrements karstiques sur les desordres survenus sur les digues de Loire dans le Val D'Orleans (France). Bull. Eng. Geol. Environ. 74 (1), 125–140. https://doi.org/10.1007/s10064-014-0594-8.

Gutiérrez, F., 2016. Sinkhole hazards. In: Oxford Research Encyclopedia of Natural Hazard Science. Oxford University Press. https://doi.org/10.1093/acrefore/9780199389407.013.40.

Gutiérrez, F., Lizaga, I., 2016. Sinkholes, collapse structures and large landslides in an active salt dome submerged by a reservoir: the unique case of the Ambal ridge in the Karun River, Zagros MountainsIran. Geomorphology 254, 88–103. https://doi.org/10.1016/j.geomorph.2015.11.020.

Gutiérrez, F., Guerrero, J., Lucha, P., 2008. A genetic classification of sinkholes illustrated from evaporite paleokarst exposures in Spain. Environ. Geol. 53 (5), 993–1006. https://doi.org/10.1007/s00254-007-0727-5.

Gutiérrez, F., Fabregat, I., Roqué, C., Carbonel, D., Guerrero, J., García-Hermoso, F., Zarroca, M., Linares, R., 2016. Sinkholes and caves related to evaporite dissolution in a stratigraphically and structurally complex setting, Fluvia Valley, eastern Spanish Pyrenees. Geological, geomorphological and environmental implications. Geomorphology 267, 76–97. https://doi.org/10.1016/j.geomorph.2016.05.018.

Gutiérrez, F., Fabregat, I., Roqué, C., Carbonel, D., Zarroca, M., Linares, R., Yechieli, Y., García-Arnay, Á., Sevil, J., 2019. Sinkholes in hypogene versus epigene karst systems, illustrated with the hypogene gypsum karst of the Sant Miquel de Campmajor Valley, NE Spain. Geomorphology 328, 57–78. https://doi.org/10.1016/j.geomorph.2018.12.003.

Hahsler, M., Piekenbrock, M., Doran, D., 2019. dbscan: Fast Density-Based Clustering with R. J. Stat. Softw. 91 (1), 1–30. https://doi.org/10.18637/jss.v091.i01.

Haliva-Cohen, A., Stein, M., Goldstein, S.L., Sandler, A., Starinsky, A., 2012. Sources and transport routes of fine detritus material to the late Quaternary Dead Sea basin. Quat. Sci. Rev. 50, 55–70. https://doi.org/10.1016/j.quascirev.2012.06.014.

Hofierka, J., Gallay, M., Bandura, P., Šašak, J., 2018. Identification of karst sinkholes in a forested karst landscape using airborne laser scanning data and water flow analysis. Geomorphology 308, 265–277. https://doi.org/10.1016/j.geomorph.2018.02.004.

Hyatt, J.A., Jacobs, P.M., 1996. Distribution and morphology of sinkholes triggered by flooding following tropical storm Alberto at Albany, Georgia, USA. Geomorphology 17 (4), 305–316. https://doi.org/10.1016/0169-555X(96)00014-1.

Ionescu, D., Siebert, C., Polerecky, L., Munwes, Y.Y., Lott, C., Häusler, S., Bižić-Ionescu, M., Quast, C., Peplies, J., Glöckner, F.O., Ramette, A., 2012. Microbial and chemical characterization of underwater fresh water springs in the Dead Sea. PLoS One 7 (6), e38319. https://doi.org/10.1371/journal.pone.0038319.

Micheletti, N., Chandler, J., Lane, S.N., 2015. Structure from motion (SFM) photogrammetry. Retrieved from. In: Clarke, L.E., Nield, J.M. (Eds.), Geomorphological Techniques, (Online Edition). http://www.geomorphology.org.uk/sites/default/files/geom_tech_chapters/2.2.2_sfm.pdf.

Mor, O., Burg, A., 2000. Geological Map of Israel, Sheet 12-III, Mizpe Shalem, 1: 50,000. Geological Survey of Israel, Jerusalem.

Neugebauer, I., Brauer, A., Schwab, M.J., Waldmann, N.D., Enzel, Y., Kitagawa, H., Torfstein, A., Frank, U., Dulski, P., Agnon, A., Ariztegui, D., 2014. Lithology of the long sediment record recovered by the ICDP Dead Sea Deep Drilling Project (DSDDP). Quat. Sci. Rev. 102, 149–165. https://doi.org/10.1016/j.quascirev.2014.08.013.

Nof, R.N., Abelson, M., Raz, E., Magen, Y., Atzori, S., Salvi, S., Baer, G., 2019. SAR Interferometry for Sinkhole early Warning and Susceptibility Assessment along the Dead SeaIsrael. Remote Sensing 11 (1), 89. https://doi.org/10.3390/rs11010089.

Panno, S.V., Luman, D.E., 2018. Characterization of cover-collapse sinkhole morphology on a groundwater basin-wide scale using lidar elevation data: a new conceptual model for sinkhole evolution. Geomorphology 318, 1–17. https://doi.org/10.1016/j.geomorph.2018.05.013.

Parise, M., 2019. Sinkholes. In: White, W.B., Culver, D.C., Pipan, T. (Eds.), Encyclopedia of Caves, 3rd edition. Academic Press, Elsevier, pp. 934–942. ISBN 978-0-12-814124-3.

Pebesma, E., 2018. Simple features for R: standardized support for spatial vector data. R J. 10 (1), 439. https://doi.org/10.32614/rj-2018-009.

Pebesma, E., 2020. Lwgeom: bindings to selected'liblwgeom'functions for simple features. R package version 2–5. Retrieved from. https://r-spatial.github.io/lwgeom/index.html.

Polom, U., Alrshdan, H., Al-Halbouni, D., Holohan, E.P., Dahm, T., Sawarieh, A., Atallah, M.Y., Krawczyk, C.M., 2018. Shear Wave Reflection Seismic Yields Subsurface Dissolution and Subrosion Patterns: Application to the Ghor Al-Haditha Sinkhole Site, Dead Sea, Jordan. https://doi.org/10.5194/se-9-1079-2018.

REDcatch GmbH, 2020. Volume calculation tool for QGIS3. Retrieved from. https://github.com/REDcatch/Volume_calculation_for_QGIS3.

Salameh, E., Alraggad, M., Amaireh, M., 2019. Degradation processes along the new northeastern shores of the Dead Sea. Environ. Earth Sci. 78 (5), 164. https://doi.org/10.1007/s12665-019-8155-x.

Schumm, S.A., 1956. Evolution of drainage systems and slopes in badlands at Perth AmboyNew Jersey. GSA Bulletin 67 (5), 597–646. https://doi.org/10.1130/0016-7606(1956)67[597:EODSAS]2.0.CO;2.

Serridge, C.J., Cooper, A.H., 2022. Natural and anthropogenic halite karst subsidence in North Cheshire, UK; comparison of Rostherne Mere, Melchett Mere, Tatton Mere and their surroundings. Q. J. Eng. Geol. Hydrogeol., qjegh2022-081 https://doi.org/10.1144/qjegh2022-081.

Shalev, E., Yechieli, Y., 2007. The effect of Dead Sea level fluctuations on the discharge of thermal springs. Isr. J. Earth Sci. 56 (1), 19–27. https://doi.org/10.1560/ijes.56.1.19.

Shalev, E., Lyakhovsky, V., Yechieli, Y., 2006. Salt dissolution and sinkhole formation along the Dead Sea shore. Journal of Geophysical Research, [Solid Earth] 111 (B3). https://doi.org/10.1029/2005JB004038.

Sneh, A., Weinberger, R., 2014. Major Structures of Israel and Environs, Scale 1: 500,000. Israel Geological Survey, Jerusalem.

Taheri, K., Gutiérrez, F., Mohseni, H., Raeisi, E., Taheri, M., 2015. Sinkhole susceptibility mapping using the analytical hierarchy process (AHP) and magnitude–frequency relationships: a case study in Hamadan provinceIran. Geomorphology 234, 64–79. https://doi.org/10.1016/j.geomorph.2015.01.005.

Team, R.C., 2022. R: A language and environment for statistical computing. R Foundation for Statistical Computing, Vienna, Austria. Retrieved from. https://www.R-project.org/.

Vey, S., Al-Halbouni, D., Haghighi, M.H., Alshawaf, F., Vüllers, J., Güntner, A., Dick, G., Ramatschi, M., Teatini, P., Wickert, J., Weber, M., 2021. Delayed subsidence of the Dead Sea shore due to hydro-meteorological changes. Sci. Rep. 11 (1), 13518. https://doi.org/10.1038/s41598-021-91949-y.

Wall, J., Bohnenstiehl, D.R., Wegmann, K.W., Levine, N.S., 2017. Morphometric comparisons between automated and manual karst depression inventories in Apalachicola National Forest, Florida, and Mammoth Cave National Park, Kentucky, USA. Nat. Hazards 85 (2), 729–749. https://doi.org/10.1007/s11069-016-2600-x.

Watson, R.A., Holohan, E.P., Al-Halbouni, D., Saberi, L., Sawarieh, A., Closson, D., Alrshdan, H., Abou Karaki, N., Siebert, C., Walter, T.R., Dahm, T., 2019. Sinkholes and uvalas in evaporite karst: spatio-temporal development with links to base-level fall on the eastern shore of the Dead Sea. Solid Earth 10 (4), 1451–1468. https://doi.org/10.5194/se-10-1451-2019.

Wickham, H., Averick, M., Bryan, J., Chang, W., McGowan, L., François, R., Grolemund, G., Hayes, A., Henry, L., Hester, J., Kuhn, M., 2019. Welcome to the tidyverse. J. Open Source Softw. 4 (43), 1686. https://doi.org/10.21105/joss.01686.

Yechieli, Y., Magaritz, M., Levy, Y., Weber, U., Kafri, U., Woelfli, W., Bonani, G., 1993. Late Quaternary Geological history of the Dead Sea AreaIsrael. Quaternary Research 39 (1), 59–67. https://doi.org/10.1006/qres.1993.1007.

Yechieli, Y., Ronen, D., Berkowitz, B., 1995. Are sedimentary salt layers always impermeable? Geophys. Res. Lett. 22 (20), 2761–2764. https://doi.org/10.1029/95gl02785.

Yechieli, Y., Kafri, U., Goldman, M., Voss, C., 2001. Factors controlling the configuration of the fresh–saline water interface in the Dead Sea coastal aquifers: Synthesis of TDEM surveys and numerical groundwater modeling. Hydrogeol. J. 9 (4), 367–377. https://doi.org/10.1007/s100400100146.

Yechieli, Y., Abelson, M., Bein, A., Crouvi, O., Shtivelman, V., 2006. Sinkhole “swarms” along the Dead Sea coast: Reflection of disturbance of lake and adjacent groundwater systems. GSA Bull. 118 (9–10), 1075–1087. https://doi.org/10.1130/B25880.1.

Yechieli, Y., Abelson, M., Baer, G., 2016. Sinkhole formation and subsidence along the Dead Sea coastIsrael. Hydrogeology Journal 24 (3), 601–612. https://doi.org/10.1007/s10040-015-1338-y.

Zilberman, T., Gavrieli, I., Yechieli, Y., Gertman, I., Katz, A., 2017. Constraints on evaporation and dilution of terminal, hypersaline lakes under negative water balance: the Dead Sea, Israel. Geochim. Cosmochim. Acta 217, 384–398. https://doi.org/10.1016/j.gca.2017.08.040.

Zumpano, V., Pisano, L., Parise, M., 2019. An integrated framework to identify and analyze karst sinkholes. Geomorphology 332, 213–225. https://doi.org/10.1016/j.geomorph.2019.02.013.